Revision 2

Experimental determination of tin partitioning between titanite, ilmenite and granitic melts using improved capsule designs

Word Count: 7609

Fangfang Huang[1,2,3], Jintuan Wang*[1,2,3], Xiaolin Xiong*[1,2,3], Mingdi Gao[1,2,3], Li Li[1,2,3], Chunxia Wei[1,2,3]

[1] State Key Laboratory of Isotope Geochemistry, Guangzhou Institute of Geochemistry, Chinese Academy of Sciences, Guangzhou 510640, China.

[2] CAS Center for Excellence in Deep Earth Science, Guangzhou, 510640, China.

[3] Southern Marine Science and Engineering Guangdong Laboratory (Guangzhou), Guangzhou 511458, China.

*Corresponding authors: wangjt@gig.ac.cn; xiongxl@gig.ac.cn

Abstract

Investigating mineral/melt Sn partitioning at high temperatures and pressures is a difficult task because Sn is a redox-sensitive multivalent element and easily alloys with noble metal sample capsules. To obtain accurate Sn partition coefficients between titanite, ilmenite, and granitic melts, we developed single capsule Pt or Au and double capsule $Pt_{95}Rh_5$ (or Au)–Re designs to avoid significant Sn loss at a controlled oxygen fugacity (fO_2). With these new capsule designs, we performed piston-cylinder experiments of Sn partitioning between titanite, ilmenite, and granitic melts. The experimental P–T–fO_2 conditions were 0.5–1.0 GPa, 850–1000 °C and ~QFM+8 to ~QFM−4 (QFM: Quartz–Fayalite–Magnetite buffer), with fO_2 controlled by the solid buffers of Ru–RuO_2, Re–ReO_2, Co–CoO, graphite, and Fe–FeO. The obtained mineral/melt Sn partition coefficients ($D_{Sn}^{\mathrm{min/melt}}$) are 0.48–184.75 for titanite and 0.03–69.45 for ilmenite at the experimental conditions. The $D_{Sn}^{\mathrm{min/melt}}$ values are largely dependent on fO_2 although the effects of temperature and melt composition are also observed. $D_{Sn}^{\mathrm{Ttn/melt}}$ strongly decreases with decreasing fO_2, from ~46–185 at the most oxidizing conditions (Ru–RuO_2 buffer), to ~2–16 at moderately oxidizing to moderately reducing conditions (Re–ReO_2 to Co–CoO and graphite buffers), to < 1 at the most reducing conditions (Fe–FeO buffer). $D_{Sn}^{\mathrm{Ilm/melt}}$ exhibits a variation trend similar to $D_{Sn}^{\mathrm{Ttn/melt}}$, but is always lower than $D_{Sn}^{\mathrm{Ttn/melt}}$ at a given fO_2. These $D_{Sn}^{\mathrm{min/melt}}$ values can be applied to quantitatively assess the mineralization potential of granitic magmas. Using $D_{Sn}^{\mathrm{Ttn/melt}}$, we estimate that Sn contents are ~150–400 ppm in the pre-mineralization magmas of the tin-mineralized Qitianling plutons (South China).

Key words: Improved capsule designs, Sn partitioning, titanite and ilmenite, oxygen fugacity

1. Introduction

Tin is a critical metal widely used in the electronics industry and decarbonization technologies (Moss et al., 2013, Lehmann, 2021). The world's tin production is dominantly from hard-rock and alluvial deposits with cassiterite (SnO_2) as the only economically important tin-bearing mineral. Both primary (hard-rock) and secondary (placer, alluvial) tin deposits are related to granites. The primary tin deposits are formed by magmatic-hydrothermal processes. They occur typically as Sn-enriched ore lodes such as greisens, hydrothermal veins, skarns, and pegmatites (Taylor 1979; Lehmann, 1990; 2021; Černý et al., 2005), and are mainly located in apical portions of granites or in wall rocks close to the granites (Lehmann, 2021). Tin-granite mineralization is often associated with small, late-stage intrusions (Lehmann, 1990; Huang et al., 2019; Lehmann, 2021). These small intrusions are always highly evolved, exhibiting extreme enrichment in incompatible elements such as volatiles (F and B), large ion lithophile elements (Li, Be, Rb, and Cs), and high field strength elements (Ta, Nb, P, and W). These features suggest that high-degree fractional crystallization is an essential step for initial Sn enrichment in the residual melt, although effective extraction, transport, and precipitation of Sn by aqueous fluids are necessary for the final formation of tin ore deposits (Zajacz et al., 2008; Audétat, 2019; Zhao et al., 2022a).

Understanding Sn metallogenic mechanisms needs knowledge of the geochemical behavior of Sn in magmatic-hydrothermal processes, which includes its valance state, species, solubility, and partitioning behavior in mineral–melt–fluid systems. In the magmatic-hydrothermal systems, Sn is present as Sn^{4+}, Sn^{2+}, or both, mainly depending on fO_2 (Linnen et al. 1995). For the behavior of Sn in fluids, the experiments of Wilson and Eugster (1990) and Schmidt (2018) demonstrated that Sn in hydrothermal solutions is transported mainly as $SnCl^+$ and $SnCl_2$ at reduced conditions, but as $SnCl_3^+$, $[SnCl_3(H_2O)_3]^+$, or $[SnCl_4(H_2O)_2]^0$ at oxidizing conditions, suggesting that Sn speciation in fluids is mainly controlled by fO_2 and fluid salinity. For the behavior of Sn in melts, solubility experiments (Linnen et al. 1995; 1996; Bhalla et al., 2005) and XAFS spectroscopy study (Farges et al., 2006) demonstrated that the Sn valance state and solubility are functions of fO_2, temperature, and melt composition. For fluid/melt partitioning of Sn, experimental investigations (Duc-Tin et al., 2007; Schmidt et al., 2020; Zhao et al., 2022b) and natural melt–fluid inclusion studies (Audétat et al., 2008; Zajacz et al., 2008) showed that Sn preferentially partitions into Cl-bearing fluids. These studies are very helpful for understanding the behavior of Sn in fluid–melt systems.

A full understanding of the behavior of Sn in magmatic-hydrothermal processes also needs the knowledge of mineral/melt partitioning coefficients of Sn ($D_{Sn}^{\mathrm{min/melt}}$). However, to our knowledge, experiments focusing on Sn partitioning are lacking mainly due to the problem of Sn alloying with noble metal sample capsules (i.e. experimental Sn loss). The alloying effect always causes severe Sn loss from the sample, resulting in false (disequilibrated) $D_{Sn}^{\mathrm{min/melt}}$ values. The lack of $D_{Sn}^{\mathrm{min/melt}}$ prevents our understanding of Sn behavior during magmatic processes, which hinders us to quantitatively assess the mineralization potential of granitic magmas. For example, the Sn contents in late-stage granitic magmas are inevitably affected by degassing and post-magmatic alteration. This is because Sn is soluble in aqueous fluids, and thus the Sn content of a crystallized granite rarely represents the Sn content of the pre-mineralization magma. However, the Sn content in the pre-mineralization magma can be quantitatively estimated if the Sn content of a mineral and its $D_{Sn}^{\mathrm{min/melt}}$ is known. Titanite and ilmenite are two Sn-rich accessory minerals in granites (Xie et al., 2010; Wang et al., 2012). Therefore, their Sn contents and $D_{Sn}^{\mathrm{min/melt}}$ can be used to assess the Sn content and mineralization potential of granitic magmas.

To obtain accurate $D_{Sn}^{\mathrm{min/melt}}$ values for titanite and ilmenite, we synthesized a tin-granite composition doped with Sn and other trace elements as the starting material. The experiments were performed in a piston-cylinder apparatus at 0.5–1.0 GPa and 850–1000 °C. As the valence state of Sn (Sn^{4+} and Sn^{2+}) mainly depends on fO_2, investigation of the effect of fO_2 on Sn partitioning is crucially important. We used the Ru–RuO_2, Re–ReO_2, Co–CoO, graphite, and Fe–FeO buffers to exert high to low fO_2 conditions. The improved capsule designs at different fO_2 buffers (see next section for details) were used to minimize the loss of Sn and consequently accurate $D_{Sn}^{\mathrm{min/melt}}$ values were obtained. The $D_{Sn}^{\mathrm{min/melt}}$ values for titanite were then used to estimate the Sn contents in the pre-mineralization tin-granites of South China.

2. Improved capsule designs

To experimentally determine accurate $D_{Sn}^{\mathrm{min/melt}}$ values, two problems must be solved. (1) Sn partitioning between minerals and melt depends largely on the valence state of Sn, which is in turn largely dependent on fO_2, and thus the experimental fO_2 has to be well controlled. (2) Sn alloying with noble metal capsules during high temperature and pressure experiments causes severe Sn loss from samples, which results in inaccurate $D_{Sn}^{\mathrm{min/melt}}$ values. Thus, the alloying effect of Sn has to be prevented.

To solve these two problems, we initially attempted to use $Au_{99}Sn_1$ capsules to avoid Sn alloying, similar to $Au_{95}Cu_5$ capsules used in Zajacz et al. (2011) and Liu et al. (2014, 2015) to avoid Cu alloying. However, only two out of more than ten runs were successful (runs 9A and 9B). In the oxidizing runs (e.g., Ru–RuO_2 or Re–ReO_2 buffers), Sn in the $Au_{99}Sn_1$ capsules was quickly oxidized to cassiterite, fracturing the capsules. In the reducing runs (e.g., graphite buffer), the Au–Sn alloying effect resulted in severe Sn loss (>90%) from sample, and this effect lowered the melting point of the alloying capsules, which caused capsule melting and experimental failure. Therefore, the $Au_{99}Sn_1$ capsule technique was abandoned in our later experiments.

Whether Sn alloys with noble metals during experiments depends on capsule material and fO_2 condition. Wang et al. (2020) investigated the alloying effect of elements with Pt capsules in piston-cylinder experiments. They found that the alloying effect of Sn with Pt is effectively prevented under the highly oxidizing conditions of the Ru–RuO_2 buffer, but under moderately oxidizing to reducing conditions ($fO_2 \leq$ Re–ReO_2 buffer), Sn–Pt alloying and Sn loss from the sample is severe. Paparoni et al. (2010) used Re capsules as sample containers to investigate Sn solubility in the Sn–SnO_2–SiO_2 system. The Re capsules in their experiments largely prevented the alloying effect of Sn due to minimal Sn solubility in Re metal (Massalski 1990). Their experiments suggest that Re capsule can be used for experiments at moderately oxidizing to reducing conditions. Based on the studies of Wang et al. (2020) and Paparoni et al. (2010), we developed new designs for single Pt or Au capsule and double capsules of $Pt_{95}Rh_5$ (or Au)–Re (see next paragraph) to perform experiments at controlled fO_2 conditions. These designs successfully solved the two problems mentioned above and enabled us to accurately determine $D_{Sn}{}^{\mathrm{min/melt}}$ at a given fO_2.

The new capsule designs for runs at a given fO_2 (buffered by Ru–RuO_2, Re–ReO_2, Co–CoO, graphite, or Fe–FeO) are shown and described in Figs. 1 a–c. The Ru–RuO_2 buffered (highly oxidizing) runs used a single capsule Pt or Au design (Fig. 1a: design 1). This capsule design works well because Sn does not alloy with noble metals under such highly oxidizing conditions and Ru does not contaminate the samples due to the negligible solubility of Ru in silicate melts. For runs buffered by Re–ReO_2, graphite, Co–CoO, or Fe–FeO buffers (i.e. at moderately oxidizing, to reducing conditions), double capsule $Pt_{95}Rh_5$ (or Au)–Re designs (Fig. 1b: design 2 and Fig. 1c: design 3) were used. In these double capsule designs, a Re capsule is used as the inner sample capsule because Sn does not alloy significantly with Re. The welded Re sample capsule is then inserted into a sintered ZrO_2 tube which was then inserted into a larger $Pt_{95}Rh_5$ (or Au) outer capsule. The ZrO_2 filler was used to reduce the deformation of the capsules during the experiment. The difference between design 2 and design 3 is the location of the fO_2 buffers. In design 2, the Re–ReO_2 or graphite buffers were loaded together with the sample into the Re capsule because Sn does not react with Re or graphite. In design 3, the Co–CoO or Fe–FeO buffers were loaded outside the Re capsule because Co and Fe may alloy with Sn and may dissolve significantly into the sample if in contact. The ZrO_2 filler in design 3 also isolates the fO_2 buffer from inner and outer metal capsules to prevent possible reaction of Co or Fe with the metal capsules.

3. Experimental and analytical methods

3.1 Starting materials and capsule preparation

A synthetic granitic composition (similar to Qitianling tin-granite, QTL38C, Huang et al., 2019) doped with a 10 wt% $CaTiSiO_5$ component, ~5000 ppm Sn, and 200–500 ppm of other trace elements (W, Mo, Nb, Ta, Zr, Hf, Li, Be, Rb, Cs, and REEs) was used as the starting material (Table 1). The addition of a $CaTiSiO_5$ component promoted titanite crystallization. To synthesize the starting material, high-purity powders of SiO_2, TiO_2, Al_2O_3, FeO, MnO, MgO, $CaCO_3$, Na_2CO_3, K_2CO_3, and trace elements were weighted and mixed in an agate mortar, then decarbonized in a Pt crucible at 1000 °C and 1 atm overnight. After that, the mixture was melted at 1500 °C for 4 hours, quenched in water, and ground to < 30 μm. Two rounds of melting–quenching–grinding procedures were performed to guarantee compositional homogeneity. Several aliquots of the final quenched glass were left for compositional analysis (Table 1). The synthesized glass powder was kept in an oven at 110 °C before use. We note that all our experiments were performed with this synthetic starting material using the above capsule designs except for two early runs (9A and 9B, as already indicated above). These two runs were performed using $Au_{99}Sn_1$ sample capsules. The starting material for these two runs was made by adding 10 wt% $CaTiSiO_5$ to a dry glass powder of the Qitianling granite (QTL38C, Huang et al., 2019) and fusing twice at 1500 °C.

For each run, the starting material and fO_2 buffers were loaded into the sample containers following designs 1–3 as shown in Figs. 1 a, b, and c. For design 1 (Ru–RuO_2 buffer), a single metal capsule (Pt or Au, 2.2–1.9 mm OD–ID and ~7 mm length) was first loaded with 3–10 wt% deionized H_2O (~0.2-0.6 mg) and then with ~4 mg Ru–RuO_2 buffer (1:1 mass ratio), followed by loading ~6 mg starting material (Fig. 1a). After that, the capsule was welded shut using a precision welding machine. For design 2 (Re–ReO_2 or graphite buffer), the inner Re capsule (2.6–1.6 mm OD–ID and ~6 mm length) was first loaded with 10–15 wt% deionized H_2O, then filled with ~7 mg Re–ReO_2 buffer (1:1 mass ratio) or graphite buffer, and then ~8 mg starting material (Fig. 1b). The inner Re capsule consists of a Re cup (made by drilling a Re cylinder with a tungsten drill bit) and a Re lid. After loading the buffer and sample, the Re cup and lid were welded together with a wet tissue used to prevent H_2O loss in an argon gas flow used to prevent Re oxidation during welding. The welded Re capsule was inserted into a sintered ZrO_2 tube, and then the $Pt_{95}Rh_5$ (or Au) outer capsule (5.0–4.7 mm OD–ID, 12 mm length). After assembling, the outer capsule was welded shut. For design 3 (Co–CoO or Fe–FeO buffer), the materials and sizes of the inner and outer capsules are almost the same as those in design 2, except that the inner Re capsule is shorter (~4 mm length) (Fig. 1c). The inner Re capsule was loaded with ~12 wt% deionized H_2O and ~6 mg starting material, and then welded shut. The Re sample capsule was inserted into a $Pt_{95}Rh_5$ (or Au) outer capsule. The space between the Re capsule and the outer capsule was then filled by the Co–CoO or Fe–FeO buffers, sintered ZrO_2 tube, and H_2O. During the preparation, all the capsules were weighed before and after welding. The welded capsules were then put into boiling water, dried in an oven (110 °C), and weighed again to double-check for leakage.

3.2 High T–P experiments

The high T–P experiments were performed in a piston-cylinder apparatus at the Guangzhou Institute of Geochemistry. The assembly (3/4 inch) consists of a talc sleeve, pyrex glass sleeve, graphite furnace, MgO inserts, and sample capsule. Experimental pressures were 0.5–1.0 GPa, with a friction correction of −22% (Liu et al., 2014). The pressure uncertainty is estimated to be < 0.1 GPa. Experimental temperatures were 850–1000 °C and measured with an S type (Pt–$Pt_{90}Rh_{10}$) thermocouple connected to a temperature controller. Temperature fluctuation was < 1 °C with respect to the set point during the experimental run. The thermocouple was not corrected for pressure. The temperature gradient within the sample capsule was estimated to be < 20 °C (Liu et al., 2014). Run durations varied from 24 to 312 hours including a time-series set of experiments. All the experiments were quenched by switching off the power to the graphite furnace. The recovered samples were mounted in epoxy resin and polished for documentation of textures and chemical analyses.

3.3 Analytical methods

Major elements in minerals and quenched glasses were analyzed with a CAMECA SX-Five electron microprobe (EPMA) at the Guangzhou Institute of Geochemistry and with a JEOL JXA-8230 EPMA at the Shandong Analysis Center of the China Metallurgical Geology Bureau. The analytical conditions were a 15 kV accelerating voltage, a 20 nA beam current, and a 1 μm beam diameter for minerals, and a 15 kV accelerating voltage, a 10 nA beam current, and a 20 μm beam diameter for the glasses. Jadeite or albite (Si, Na), rutile (Ti), yttrium Al garnet (Al), olivine (Fe, Mg), rhodonite (Mn), diopside (Ca), and sanidine (K) were used as the standards. An anhydrous basaltic glass (XT-168, Xiong et al., 2005; Li et al., 2017) and the NIST-610 glass were used as the monitor standards. All the data were corrected using ZAF correction procedures. Analytical accuracy for major elements was better than 1% relative for SiO_2 and Al_2O_3, 2% for MgO, FeO, CaO, and K_2O, and 5% for TiO_2. Because Na loss occurs during EPMA analysis of hydrous glasses, the reported Na_2O contents in quench glasses are from the LA-ICP-MS analyses.

Trace elements (Sn and other trace elements) and Na_2O contents in quenched glasses were measured with an ELEMENT XR (Thermo Fisher Scientific) ICP-SF-MS coupled to a 193 nm (ArF) Resonetics RESOlution M-50 laser ablation system (LA-ICP-MS) at the Guangzhou Institute of Geochemistry. The analytical conditions were set to ~4 J cm^{-2} energy density at the sample surface, 6Hz repetition rate, and beam sizes of 17–32 μm. NIST-610, NIST-612, BCR-2G, and BHVO-2G were used as the external standards, and GSD-1G was used as the monitor standard. EPMA analyzed Si content was used as the internal standard. The analytical accuracy and precision were better than 10% relative for Sn and Na and most other elements. Details of the method are reported in Zhang et al. (2019). Because minerals in the run products are small (mostly < 30 μm for titanite and < 15 μm for ilmenite), their trace element contents cannot be analyzed by LA-ICP-MS. Therefore, we analyzed trace element contents in minerals with EPMA at high beam currents and long peak counting times. The analytical conditions were set to a 15 kV accelerating voltage, a 80 nA beam current, a 1–2 μm beam diameter, and peak counting times of 60–120 s. To investigate whether there was Sn-loss from our sample capsules, the capsule walls were also analyzed using this high beam current method. For the analyses of minerals and metal capsules, monazite, glasses, and metals (Sn, Nb, Ta, W, Mo, Zr, Hf, Pt, Re, and REEs) were used as the standards.

To examine the accuracy of the EPMA Sn analyses, we also measured Sn in the quenched glasses using the same high beam current condition (80 nA) as for the minerals. A comparison between the EPMA and LA-ICP-MS results for the quenched glasses shows excellent agreement between the two methods for Sn contents > ~300 ppm (Fig. 2), demonstrating the reliability of the EPMA Sn analysis of our samples. Because the Sn contents in titanite and ilmenite are generally higher than 300 ppm, we believe that the EPMA determined Sn contents in the minerals are accurate.

4. Results

4.1. Run products and experimental *f*O$_2$

Twenty-two experiments were conducted at 850–1000 °C and 0.5–1.0 GPa, including 16 runs buffered to highly oxidizing condition (Ru–RuO$_2$ buffer), 1 run buffered at moderately oxidizing condition (Re–ReO$_2$ buffer), and 5 runs buffered at reducing conditions (graphite, Co–CoO, or Fe–FeO buffers). The experimental conditions (T–P–*f*O$_2$), run products, phase proportions, and estimated Sn- and Fe-loss are reported in Table 2. All buffers (examined by SEM, as shown in Fig. 3) survived the duration of the experiments except for the Fe–FeO buffered run, in which the Fe metal was entirely consumed. However, we consider this run to have been very reducing because its $D_{Sn}^{\mathrm{Ttn/melt}}$ is the lowest of all the runs (see section 5.2). Each run product contains 3–6 phases, including titanite (in 17 runs), ilmenite (all runs), rutile (2 runs), clinopyroxene (5 runs), scheelite (4 runs), hematite (1 run), cassiterite (17 runs), quenched glass (all runs), and fluid bubbles (17 runs) (Table 2). Titanite crystals in most runs have euhedral to subhedral envelope shapes (Figs. 3 a and c). They are generally < 20–30 μm, except for runs T5A and T5B, where titanite grains are up to 40–80 μm. Ilmenite and hematite grains are subhedral and generally < 10 μm (Figs. 3 a, b, and c). Clinopyroxene is euhedral and < 40 μm. Cassiterite (< 5 μm) is present only in the moderately to highly oxidizing runs buffered by Ru–RuO_2 and Re–ReO_2. Rutile (< 5 μm) is present as needle-shaped crystals in one of the graphite and one of the Re–ReO_2 buffered runs. Scheelite (< 10 μm) is present in 4 runs due to tungsten contamination of the Re capsules because they were made using a tungsten drill bit. Quenched glasses in all the run products are clear as shown in Fig. 3. The quenched glasses in 17 runs (except for 9A, 9B, and the graphite buffered runs, Table 2) contain round fluid bubbles (Table 2), which together with the analytical results indicates melt H_2O saturation during the experiments.

The phase proportions, Fe-loss, and Sn-loss were calculated by mass balance (Table 2). For the cassiterite-saturated runs, we cannot assess Sn-loss because Sn-loss in these runs is correlated with the estimated proportions of cassiterite, which is largely uncertain. Therefore, we only calculated the Sn-loss for the cassiterite unsaturated runs. The proportions of quenched glasses and crystalline phases are 85.3–98.8 wt% and 1.2–14.7 wt%, respectively. The absence of titanite ($CaTiSiO_5$) in five runs may be due to the high temperature of 1000 °C (e.g., runs 7M, 7D, and 28Re) or low melt CaO concentrations caused by the crystallization of clinopyroxene and/or scheelite (e.g., runs 22Re and 21Re). Importantly, mass balance calculations show no significant Fe loss (0–3 wt% relative) and Sn loss (0–3.8 wt% relative) for all calculated runs except two runs (10Re, buffered by Co–CoO; and 12Re, buffered by Fe–FeO), where approximately 50% Sn was lost from the samples (Table 2). The EPMA analysis of the capsule walls (Table S1) shows that Sn contents of the Re capsules (<50 ppm) are less than half of the detection limit (90 ppm), suggesting insignificant Sn loss from the samples to the Re capsule walls. Therefore, we infer that Sn partitioned into the fluids in runs 10Re and 12Re, which did not affect the determined $D_{Sn}^{\mathrm{min/melt}}$ partition coefficients because the fluid/melt easily reaches equilibrium relative to the mineral/melt.

The experimental fO_2 values were calculated based on the equations of the fO_2 buffers. In the runs conducted with capsule designs 1 and 2 (Figs. 1 a and b), the buffers were directly in contact with the samples. fO_2 values in these runs were calculated according to O’Neill and Nell (1997) for Ru–RuO_2, Pownceby and O’Neill (1994) for Re–ReO_2, and Jakobsson and Oskarsson (1994) for graphite. In runs with capsule design 3 (Fig. 1c), the fO_2 values were calculated following Holmes et al. (1986) for Co–CoO, and Huebner (1971) for Fe–FeO, because both the inner sample capsule and the outer buffer-containing capsule were water-saturated. The calculated results (Table 2) show that the relative fO_2 values vary from QFM+8.1 (i.e., 8.1 log units above the Quartz–Fayalite–Magnetite buffer) to ~QFM−4.2 under the experimental P–T conditions.

4.2 Compositions and Sn contents of titanite and ilmenite

The composition and Sn contents of the titanite and ilmenite are presented in Tables 3–4 and Tables S2–S3. Titanite consists of SiO_2 (26.1–29.6 wt%), TiO_2 (25.2–36.1 wt%), and CaO (23.0–25.6 wt%) with minor Al_2O_3 (0.7–1.5 wt%), FeO (1.2–4.0 wt%), REE_2O_3 (total 3.3–9.0 wt%, including La_2O_3, Ce_2O_3, Pr_2O_3, Sm_2O_3, Eu_2O_3, Gd_2O_3, Dy_2O_3 and Yb_2O_3), Nb_2O_5 (0.3–0.8 wt%), Ta_2O_5 (0.4–0.7 wt%), WO_3 (0.5–0.9 wt%), ZrO_2 (0.2–0.4 wt%), and HfO_2 (0.3–0.7 wt%). SnO_2 in titanite varies from 0.14 to 15.14 wt%, which increases with increasing fO_2. For single runs, SiO_2, TiO_2 and CaO in titanite are generally homogeneous, but in the oxidized runs, SnO_2 in titanite shows slight zoning (Tables 3 and S2). For most of these runs, the SnO_2 content in the titanite rims (6–10 wt%) is lower than that in the cores (8–14 wt%), except for runs 9A and 9B. In these two runs, the Sn content in the rims is higher than that in the cores owing to the use of $Au_{99}Sn_1$ capsules as the Sn source. For all the runs, we only used the rim compositions to calculate the $D_{Sn}^{\mathrm{Ttn/melt}}$ values.

The composition of the ilmenite is homogeneous in single runs. Ilmenite is mainly composed of FeO_T (39.8–68.7 wt%), TiO_2 (10.3–53.9 wt%), MgO (1.1–4.7 wt%), MnO (0.1–0.6 wt%), Al_2O_3 (0.1–1.9 wt%), and SnO_2 (0.02–5.60 wt%) (Tables 4 and S3). The composition of the ilmenite can be described by end member wüstite (FeO), hematite ($FeO_{1.5}$), and rutile (TiO_2). Based on stoichiometry, we calculated

FeO and $FeO_{1.5}$ contents for ilmenite, and then assigned MgO and MnO to wüstite, $AlO_{1.5}$ to hematite, and SnO_2 to rutile. The calculated compositions were plotted on the ternary wüstite–hematite–rutile diagram (Fig. 4), showing that all compositions are located on the solid solution join of ilmenite and hematite with compositions ranging from $Ilm_{100}Hem_0$ to Ilm_8Hem_{92}. Ilmenite in run 9A, with the highest FeO_T (68.7 wt%) concentration, approaches the hematite end member composition (Table 4).

We also report the compositions and Sn contents of rutile and clinopyroxene (Table 4 and Tables S3–S4). Rutile contains 68.2–88.3 wt% TiO_2 and 0.06–17.52 wt% SnO_2. Clinopyroxene has a $En_{31–37}$, $Fs_{13–20}$, $Wo_{48–50}$ composition, which contains 0.01–1.04 wt% SnO_2. Cassiterite and scheelite compositions are given in Table S5.

4.3 Compositions, Sn contents, and H_2O contents of quenched glasses

The compositions and Sn contents of the quenched glasses are reported in Tables 5 and S6. Major element oxides SiO_2, Al_2O_3, MgO, Na_2O, and K_2O (except TiO_2, FeO, and CaO) are generally similar to those in the starting material due to the low degrees of crystallization (< 15 wt%). The changes in TiO_2 (0.2–3.4 wt% in glasses vs. 4.1 wt% in starting material), FeO (0.8–4.1 wt% in glasses vs. 5.4 wt% in starting material), and CaO (slight decrease in some glasses relative to starting material) were caused by the crystallization of ilmenite, titanite, and clinopyroxene. The melt polymerization degree is expressed by NBO/T (non-bridging oxygens per tetrahedrally coordinated cation). Values were calculated as NBO/T = $(2 \cdot X_O$-

$4 \cdot X_T)/X_T$, where X_T and X_O are the atomic proportions of tetrahedrally coordinated cations (Si, Al, Fe^{3+}) and total oxygen (Mysen and Richet, 2019), respectively. The total oxygen was calculated from the SiO_2, TiO_2, Al_2O_3, FeO, Fe_2O_3, MnO, MgO, CaO, Na_2O, K_2O, and SnO_2 contents. According to Honada and Soga (1980), Ti tends to be a network-modifier when TiO_2 is < 10 wt% in the melt. Therefore, among the cations above, Ti, Fe^{2+}, Mn, Mg, Ca, Na, K, and Sn were regarded as network-modifying ions. The Fe^{3+}/Fe_T ratios and Fe^{3+} in the melt were calculated according to the equation (A6) of Kress and Carmichael (1991). The calculated NBO/T values range from 0.035 to 0.364. Tin contents in the quenched glasses are ~330–6700 ppm as measured by LA-ICP-MS, and ~300–7200 ppm as measured by EPMA (Tables 5 and S6).

H_2O contents for most of the quenched glasses were estimated using the EPMA by-difference method (calculated by 100 minus the EPMA total) because most of the quenched melts contain tiny fluid bubbles, making the double-polished sample wafers opaque and impossible for FTIR (Fourier transform infrared spectrometer) analyses. We have demonstrated in our recent work (Xu et al., 2022; Gao et al., 2023) that, for H_2O-rich glasses, the melt H_2O contents estimated from the by-difference method are comparable to that measured by FTIR within an ~10% uncertainty. We also analyzed H_2O contents in two H_2O-unsaturated samples (runs 22Re and 28Re buffered by graphite, Tables 2 and S7) by FTIR following the procedures of Xu et al., (2022) and Gao et al. (2023). The melt H_2O contents measured by FTIR are 3.1wt% for run 22Re and 2.1 wt% for run 28Re (Table S7), consistent with that estimated from the EPMA by-difference method (3.1 wt% for run 22Re and 1.8 wt% for run 28Re, Table S7), further confirming the reliability of the EPMA by-difference method. For the EPMA by-difference method, the estimation of melt H_2O content requires accurate EPMA totals of glass. However, the EPMA analysis of hydrous glasses usually suffers Na loss, leading to under-estimated EPMA totals. Therefore, we used Na contents determined by LA-ICP-MS to correct the EPMA totals. The melt H_2O contents estimated via EPMA by-difference are 7.3–12.0 wt% except for three graphite buffered runs (< 6.0 wt% H_2O in glass) (Table 5).

Compared to the initially added H_2O contents, the glass H_2O contents vary in different ways depending on the capsule design (Table 5). Relative to the initially added H_2O content, the glass H_2O content generally increases in design 1 (Ru–RuO_2 buffered runs), decreases in design 2 (graphite buffered runs), and remains almost unchanged in design 3 (Co–CoO or Fe–FeO buffered runs) (Fig. 1). The H_2O contents in the quenched glasses represent the melt H_2O contents. The change in the melt H_2O content indicates H_2 diffusion (through different metal capsule walls) and H_2O formation or decomposition during the experiments. In design 1, the Ru–RuO_2 buffer is in direct contact with the sample, leading to extremely high fO_2 and low fH_2 (Fig. 1a). In this case, H_2 continually diffused into the sample capsule (Pt or Au) and reacted with RuO_2 to form H_2O ($2H_2 + RuO_2 = 2H_2O + Ru$), resulting in melt H_2O increase and saturation. In design 2, the graphite buffer is in direct contact with the sample, leading to low fO_2 and high fH_2 (Fig. 1b). In this case, H_2 diffused out of the sample capsule (Re), resulting in H_2O decomposition ($H_2O = H_2 + 1/2O_2$) and melt H_2O content decrease. In design 3, the reducing Co–CoO or Fe–FeO buffers were located outside the sample capsule (Re) (Fig. 1c). In this design, melt H_2O content should increase because H_2 diffuses into the sample capsule (Re) and reacts with Fe_2O_3 or SnO_2 to form H_2O. However, we did not observe a significant change in the melt H_2O content compared to the initially added H_2O content because both the inner sample capsule (Re) and outer buffer contained capsule ($Pt_{95}Rh_5$ or Au) were H_2O-saturated during the experiments.

5. Discussion

5.1 Evaluation of Equilibrium

Evaluation of Sn partitioning equilibrium should consider its valence states (Sn^{4+} and Sn^{2+}). For the same experimental duration, Sn^{2+} should have reached diffusion and partitioning equilibrium if Sn^{4+} approached equilibrium because Sn^{4+} diffuses much slower than Sn^{2+} (Linnen et al. 1995, 1996). In this study, we assessed the partitioning equilibrium of Sn^{4+} by conducting time-series experiments and using the Sn solubility in melt at cassiterite saturation in the Ru–RuO_2 buffered runs. Such a high fO_2 buffer (~QFM+8 at our run conditions) should result in Sn present as Sn^{4+} in the experimental charges (Linnen et al. 1995). The time-series experiments (900 °C, 0.5 GPa) include 6 runs with durations of 24, 48, 72, 96 hours and 2 runs with a duration of 120 hours (Table 2). The results show that $D_{Sn}^{\mathrm{Ttn/melt}}$ is 79 (± 12) for the 24h run, decreases to 65–68 for the 48h runs, and remains almost constant at 60 (± 5) for the 72h to 120h runs (Fig 5a; Table 6), suggesting that titanite/melt Sn partitioning approaches equilibrium at ≥ 72h under these experimental conditions. Therefore, only the $D_{Sn}^{\mathrm{Ttn/melt}}$ from ≥ 72h runs are used in the later discussion. For ilmenite, $D_{Sn}^{\mathrm{Ilm/melt}}$ is 21(±1.7) from 24h to 120h runs, showing that Sn partitioning between ilmenite and melt approaches equilibrium rapidly (Fig 5a; Table 6).

The dissolution equilibrium of cassiterite can be inferred from the melt Sn contents in the cassiterite saturated runs at the Ru–RuO_2 buffered condition. For these runs, Sn solubility increases from 326 ppm at 850 °C to 2454 ppm at 1000 °C (Fig 5b; Table 5). The near linear increase of Sn solubility with temperature indicates that Sn dissolution approaches equilibrium. In addition, the Sn solubility of 326(±14) to 466 (±22) ppm determined for our experiments at 850 °C, 0.5 GPa, and QFM+8 compares within error to the SnO_2 solubility data of Linnen et al. (1995) at 850 °C, 2 kbar, and QFM+3.1 (800±390 ppm SnO_2 equivalent to 632±308 ppm Sn), further indicating that our experiments reached or closely approached equilibrium.

5.2 Mineral/melt Sn partition coefficients

Mineral/melt Sn partition coefficients ($D_{Sn}^{\mathrm{min/melt}}$) were calculated from the Sn contents in minerals (by EPMA) and in melts (by LA-ICP-MS), and are reported in Tables 6 and S8. The results include 14 values for titanite ($D_{Sn}^{\mathrm{Ttn/melt}}$), 22 values for ilmenite ($D_{Sn}^{\mathrm{Ilm/melt}}$), 2 values for rutile ($D_{Sn}^{\mathrm{Rtl/melt}}$), and 5 values for clinopyroxene

($D_{Sn}^{\mathrm{Cpx/melt}}$).

The D_{Sn} values for titanite/melt are 0.48–185 in our experimental conditions (850–1000 °C, 0.5–1.0 GPa, fO_2 = ~QFM+8 to ~QFM−4). $D_{Sn}^{\mathrm{Ttn/melt}}$ strongly decreases with decreasing fO_2 (Fig. 6a, Tables 2, 6, and S8a), from ~46–185 under the most oxidizing conditions (Ru–RuO$_2$ buffer), then ~2–16 under the moderately oxidizing to moderately reducing conditions (Re–ReO$_2$ to Co–CoO and graphite buffers), to < 1 at the most reducing conditions (Fe–FeO buffer). For the Ru–RuO$_2$ buffered runs, the effects of temperature and/or melt NBO/T are also observable. As shown in Figs. 6b and 6c, $D_{Sn}^{\mathrm{Ttn/melt}}$ increases with decreasing temperature and melt NBO/T. Regression of our $D_{Sn}^{\mathrm{Ttn/melt}}$ data obtained the following relation from $D_{Sn}^{\mathrm{Ttn/melt}}$, fO_2 (ΔQFM), and temperature (K) (data in Table S9a):

$$\mathrm{Ln}D_{Sn}^{\mathrm{Ttn/melt}} = 0.39*(\Delta\mathrm{QFM}) + 6511/T - 4.1\ (R^2=0.96) \quad (1).$$

Melt NBO/T is not considered in the equation because its effect is indistinguishable from that of temperature.

The D_{Sn} values for ilmenite/melt are 0.03–69 (Tables 6 and S8b), which is lower than those for titanite (0.48–185) at a given fO_2. Similar to $D_{Sn}^{\mathrm{Ttn/melt}}$, $D_{Sn}^{\mathrm{Ilm/melt}}$ also strongly decreases with decreasing fO_2 (Fig. 6d), and slightly increases with decreasing temperature (Fig. 6e) and/or melt NBO/T (Fig. 6f). We note that $D_{Sn}^{\mathrm{Ilm/melt}}$ in the Fe–FeO buffered run deviates from the D_{Sn}–fO_2 trend (Fig. 6d). Thus we did not fit the $D_{Sn}^{\mathrm{Ilm/melt}}$ as a function of fO_2, T, and melt composition. Considering the rapid equilibrium of Sn partitioning between ilmenite and melt, we infer that the deviation may have resulted from fO_2 fluctuation in the charge caused by the consumption of Fe metal in the Fe–FeO buffer. However, consumption of the Fe metal seems to have no significant effect on $D_{Sn}^{\mathrm{Ttn/melt}}$ (Fig. 6a). This may indicate that titanite in this run formed during the latest stage when large fO_2 fluctuations had stopped in the charge.

The two D_{Sn} values for rutile/melt and five D_{Sn} values for clinopyroxene/melt are 0.09–20.0 and 0.01–17.5, respectively (Tables S8b–c). D_{Sn} values for the two minerals also strongly decrease with decreasing fO_2.

5.3 Substitution mechanisms of Sn in titanite and ilmenite

Understanding the substitution mechanism of Sn in a mineral is the basis for understanding its partitioning behavior. The substitution mechanisms of Sn in titanite and ilmenite should be controlled by the composition and structure of the titanite and ilmenite, as well as the valance state, ionic radius (Å) and coordination number of Sn. Titanite ($CaTiSiO_5$) has a monoclinic crystal structure, where Ca^{2+} and Ti^{4+} have VII and VI coordination numbers (CN), respectively. Eremin et al. (2002) pointed out that Ti^{4+} ($^{VI}Ti^{4+}$: 0.61 Å, Shannon 1976) in titanite can be fully replaced by Sn^{4+} ($^{VI}Sn^{4+}$: 0.69 Å), forming the $CaSnSiO_5$ end member (malayaite). Ilmenite ($(Fe,Ti)_2O_3$) has a hexagonal structure, where both Fe^{2+} and Ti^{4+} have VI CN. Considering the similar ionic radius and the same CN of Sn^{4+} and Ti^{4+}, we infer that Sn^{4+} may also replace Ti^{4+} in ilmenite.

Tin in silicate melts is present as Sn^{4+}, Sn^{2+}, or both, depending mainly on fO_2 (Linnen et al. 1995; 1996; Bhalla et al., 2005; Farges et al., 2006). The Sn solubility experiments of Linnen et al. (1995) indicate that Sn in the melt is present exclusively as Sn^{4+} at fO_2 > ~QFM+3. In our Ru–RuO_2 buffered runs, the fO_2 values are ~QFM+8, and Sn should be Sn^{4+} in the melts. For these runs, we expect a positive correlation between D_{Sn} and D_{Ti} due to the substitution of $Sn^{4+} \leftrightarrow Ti^{4+}$.

In this study, we also report the D_{Ti} values for ilmenite and titanite in addition to D_{Sn} (Tables S8a–b) and plot D_{Sn} vs. D_{Ti} in Fig. 7. As shown in this figure, D_{Sn} and D_{Ti} indeed exhibit a good positive correlation for the Ru–RuO_2 buffered runs, confirming the substitution of $Sn^{4+} \leftrightarrow Ti^{4+}$ in titanite and ilmenite. In our experiments, the Sn^{4+} content in the melts should decrease and the Sn^{2+} content increase with decreasing fO_2 (from the Ru–RuO_2 and Re–ReO_2, buffers to the Co–CoO buffer to the graphite and Fe–FeO buffers). The strong decrease in D_{Sn} with decreasing fO_2 (Figs. 6 a and d) suggests that Sn^{2+} is highly incompatible in titanite and ilmenite. The study of Sidey (2022) suggested that Sn^{2+} in titanite and ilmenite is mainly present as CN = VI (1.02 Å) and CN = VIII (1.17 Å), but a CN = VII for Sn^{2+} has never been reported. In titanite, $^{VI}Sn^{2+}$ cannot enter the $^{VI}Ti^{4+}$ (0.61 Å) site because its ionic radius (1.02 Å) is much larger than $^{VI}Ti^{4+}$. It seems that Sn^{2+} also cannot enter the Ca^{2+} site because Ca^{2+} is VII–coordinated, but Sn^{2+} lacks this coordination number. In ilmenite, Sn^{2+} cannot enter either the $^{VI}Ti^{4+}$ (0.61 Å) site or the $^{VI}Fe^{2+}$ (0.78 Å) site because the ionic radius of $^{VI}Sn^{2+}$ (1.02 Å) is much larger than those of $^{VI}Ti^{4+}$ and $^{VI}Fe^{2+}$. In summary, the substitution mechanisms discussed above largely explain the partitioning behaviors of Sn between titanite, ilmenite, and melt, especially with respect to the effect of fO_2.

6. Implications

The Sn contents of magmas can provide useful information regarding the mineralization potential of tin-granites. However, the Sn content of the bulk rocks rarely represents that of the pre-mineralization magma because the Sn content in a primitive magma may change during magmatic degassing and/or post magmatic alteration. During magmatic crystallization, Sn partitions between the crystallizing phases and the melt. The Sn content of a mineral can therefore be used to estimate Sn content of the coexisting melt if the mineral/melt D_{Sn} is known. In this study, we obtained $D_{Sn}^{\mathrm{min/melt}}$ values for titanite and ilmenite. However, ilmenite is in most cases not suitable for estimating the Sn content of the equilibrium melts, especially for magmas that have slowly crystallized to granites because ilmenite easily re-equilibrates at sub-solidus conditions (Bacon and Hirschmann, 1988; Hou et al., 2020). In contrast, titanite is ideal for estimating the magmatic Sn content because it is relatively inert during post-magmatic alteration (Xie et al., 2010; Che et al., 2013).

As an example, we used the $D_{Sn}^{\mathrm{Ttn/melt}}$ data to estimate the magmatic Sn contents of the Qitianling granites. The Sn-mineralized Qitianling granites in southern China contain magmatic titanite in the hornblende-biotite (Hbl-Bt) granite and biotite (Bt) granite. Xie et al. (2008, 2010) reported 0.15 wt% and 0.43 wt% Sn on average in titanite from the Hbl-Bt granite and the Bt-granite, respectively. They also determined an average crystallization temperature of 750 °C for the Bt granite using the Zr-in-titanite thermometry of Hayden et al. (2007). Huang et al. (2019) estimated a crystallization temperature of 820 °C for the Hbl-Bt granite using the hornblende-plagioclase thermometry of Holland and Blundy (1994). In addition, Huang et al. (2019) conducted phase equilibria modelling and obtained an fO_2 of $\sim\Delta$NNO-1 ± 0.5 for the Qitianling granites. Based on the titanite Sn content, temperature, fO_2, and equation (1) presented in section 5.2, we estimated Sn contents in the Hbl-Bt granitic and Bt granitic magmas before degassing. The results show that the primitive Hbl-Bt granitic and Bt granitic magmas contained 149–219 ppm and 276–406 ppm Sn, respectively (Fig. 8, Table S9b). Compared to Sn contents in melt inclusions (~10–~550 ppm) of tin-granites elsewhere (Audétat et al., 2000; Zajacz et al., 2008; Borisova et al., 2012, Fig. 8), the estimated melt Sn contents for the Qitianling tin-granites are at the high end, indicating that the primitive magmas (or melts) of the Qitianling granites were Sn-rich. The Qitianling granites have bulk rock Sn contents of ~25 ppm on average (Xie et al., 2010; Huang et al., 2019), much lower than those estimated for the melts from the pre-mineralization magmas. The bulk rock Sn contents are thus not a reliable proxy for the mineralization potential of the magma.

Acknowledgements and funding

We would like to thank Wenlan Zhang, Pengli He, Yonghua Cao, Shuang Xu, Tengda Guo for the assistance in EPMA analyses, Le Zhang for the assistance in LA-ICP-MS analyses, and Saskia Erdmann and Bin Fu for discussions and help with language. Comments and suggestions by Robert Linnen, Zoltan Zajacz and an anonymous reviewer are appreciated. We also thank Daniel Harlov for his editorial handling. This work was financially supported by the National Natural Science Foundation of China (Grant No. 41921003, 92062222, 42003046, 42250202), the China Postdoctoral Science Foundation project (2019M663135) and the opening funding of State Key Laboratory for Mineral Deposits Research, Nanjing University (2020-LAMD-K06).

Supplementary data

Supplementary tables data of this study (including all the trace element data) are available from the Figshare Repository:

DOI: https://doi.org/10.6084/m9.figshare.25184018

References cited

Audétat A., Pettke T., Heinrich C. A. and Bodnar, R. J. (2008) The composition of magmatichydrothermal fluids in barren and mineralized intrusions. Economic Geology 103, 877-903.

Audétat, A. (2019) The Metal Content of Magmatic-Hydrothermal Fluids and Its Relationship to Mineralization Potential. Economic Geology 114, 1033-1056.

Audetat, A., Gunther, D. and Heinrich, C.A. (2000) Magmatic-hydrothermal evolution in a fractionating granite: A microchemical study of the Sn-W-F-mineralized Mole Granite (Australia). Geochimica Et Cosmochimica Acta 64, 3373-3393.

Bacon, C.R. and Hirschmann, M.M. (1988) Mg/Mn Partitioning as a Test for Equilibrium between Coexisting Fe-Ti Oxides. American Mineralogist 73, 57-61.

Bhalla, P., Holtz, F., Linnen, R.L. and Behrens, H. (2005) Solubility of cassiterite in evolved granitic melts: effect of T, fO_2, and additional volatiles. Lithos 80, 387-400.

Borisova, A.Y., Thomas, R., Salvi, S., Candaudap, F., Lanzanova, A. and Chmeleff, J. (2018) Tin and associated metal and metalloid geochemistry by femtosecond LA-ICP-QMS microanalysis of pegmatite–leucogranite melt and fluid inclusions: new evidence for melt–melt–fluid immiscibility. Mineralogical Magazine 76, 91-113.

Černý, P., Blevin, P.L., Cuney, M., London, D., 2005. Granite-related ore deposits.

Economic Geology 100th Anniversary 337–370.

Che, X.D., Linnen, R.L., Wang, R.C., Groat, L.A. and Brand, A.A. (2013) Distribution of Trace and Rare Earth Elements in Titanite from Tungsten and Molybdenum Deposits in Yukon and British Columbia, Canada. The Canadian Mineralogist 51, 415-438.

Duc-Tin, Q., Audétat, A. and Keppler, H. (2007) Solubility of tin in (Cl, F)-bearing aqueous fluids at 700 °C, 140MPa: A LA-ICP-MS study on synthetic fluid inclusions. Geochimica et Cosmochimica Acta 71, 3323-3335.

Eremin, N.N., Urusov, V.S., Rusakov, V.S. and Yakubovich, O.V. (2002) Precision X-ray diffraction and Mössbauer studies and computer simulation of the structure and properties of malayaite $CaSnOSiO_4$. Crystallography Reports 47, 759-767.

Farges, F., Linnen, R.L. and Brown, G.E. (2006) Redox and speciation of tin in hydrous silicate glasses: A comparison with Nb, Ta, Mo and W. Can Mineral 44, 795-810.

Frost, B.R. (1991) Introduction to Oxygen Fugacity and Its Petrologic Importance. Rev Mineral 25, 1-9.

Gao, M.D., Xiong, X.L., Huang, F.F., Wang, J.T., and Wei, C.X. (2023) Key factors controlling biotite–silicate melt Nb and Ta partitioning: Implications for Nb-Ta enrichment and fractionation in granites. Journal of Geophysical Research: Solid Earth, 128, e2022JB025889. https://doi. org/10.1029/2022JB025889.

Hayden, L.A., Watson, E.B. and Wark, D.A. (2007) A thermobarometer for sphene (titanite). Contributions to Mineralogy and Petrology 155, 529-540.

Holland, T. and Blundy, J. (1994) Nonideal Interactions in Calcic Amphiboles and Their Bearing on Amphibole-Plagioclase Thermometry. Contributions to Mineralogy and Petrology 116, 433-447.

Holmes, R.D., O'Neill, H.S.C. and Arculus, R.J. (1986) Standard Gibbs free energy of formation for Cu_2O, NiO, CoO, and Fe_xO: High resolution electrochemical measurements using zirconia solid electrolytes from 900–1400 K. Geochimica et Cosmochimica Acta 50, 2439-2452.

Honada, T. and Soga, N. (1980) Coordination of titanium in silicate glasses. J. Noncrystall. Solids, 38, 105-110.

Hou, T., Botcharnikov, R., Moulas, E., Just, T., Berndt, J., Koepke, J., Zhang, Z., Wang, M., Yang, Z. and Holtz, F. (2020) Kinetics of Fe–Ti Oxide Re-equilibration in Magmatic Systems: Implications for Thermo-oxybarometry. Journal of Petrology 61.

Huang, F., Scaillet, B., Wang, R., Erdmann, S., Chen, Y., Faure, M., Liu, H., Xie, L., Wang, B. and Zhu, J. (2019) Experimental Constraints on Intensive Crystallization Parameters and Fractionation in A-Type Granites: A Case Study on the Qitianling Pluton, South China. Journal of Geophysical Research: Solid Earth 124, 10132-10152.

Huebner, I.S. (1971) Buffering techniques for hydrostatic systems at elevated pressures. In Ulmer, G. C. Research Techniques for High Pressures and High Temperatures. Springer-Verlag, New York, 123-177.

Jakobsson, S. and Oskarsson, N. (1994) The System C-O in Equilibrium with Graphite at High-Pressure and Temperature - an Experimental-Study. Geochimica Et Cosmochimica Acta 58, 9-17.

Kress, V.C. and Carmichael, I.S.E. (1991) The compressibility of silicate liquids containing Fe2O3 and the effect of composition, temperature, oxygen fugacity and pressure on their redox states. Contributions to Mineralogy and Petrology 108, 82-92.

Lehmann, B. (2021) Formation of tin ore deposits: A reassessment. Lithos 402.

Lehmann, B., (1990) Metallogeny of Tin. Springer, Berlin, p. 211.

Li, L., Xiong, X.L. and Liu, X.C. (2017) Nb/Ta Fractionation by Amphibole in Hydrous Basaltic Systems: Implications for Arc Magma Evolution and Continental Crust Formation. Journal of Petrology 58, 3-28.

Linnen, R.L., Pichavant, M. and Holtz, F. (1996) The combined effects of fO_2 and melt composition on SnO2 solubility and tin diffusivity in haplogranitic melts. Geochimica et Cosmochimica Acta 60, 4965-4976.

Linnen, R.L., Pichavant, M., Holtz, F. and Burgess, S. (1995) The effect of fO_2 on the solubility, diffusion, and speciation of tin in haplogranitic melt at 850 °C and 2 kbar. Geochimica et Cosmochimica Acta 59, 1579-1588.

Liu, X., Xiong, X., Audétat, A. and Li, Y. (2015) Partitioning of Cu between mafic minerals, Fe–Ti oxides and intermediate to felsic melts. Geochimica et Cosmochimica Acta 151, 86-102.

Liu, X., Xiong, X., Audétat, A., Li, Y., Song, M., Li, L., Sun, W. and Ding, X. (2014) Partitioning of copper between olivine, orthopyroxene, clinopyroxene, spinel, garnet and silicate melts at upper mantle conditions. Geochimica et Cosmochimica Acta 125, 1-22.

Mallmann, G. and O'Neill, H.S.C. (2007) The effect of oxygen fugacity on the partitioning of Re between crystals and silicate melt during mantle melting. Geochimica et Cosmochimica Acta 71, 2837-2857.

Moss, R., Tzimas, E., Willis, P., Arendorf, J., Tercero Espinoza, L., et al., 2013. Critical metals in the path towards the decarbonisation of the EU energy sector. Assessing rare metals as supply-chain bottlenecks in low-carbon energy technologies. Scientific and Policy report, Joint Research Centre, European Commission. Publications Office, Luxemburg, p. 242.

Mysen, B., and Richet, P. (2019). Silicate glasses and melts. Elsevier.

O'Neill, H.S.C. and Eggins, S.M. (2002) The effect of melt composition on trace element partitioning: an experimental investigation of the activity coefficients of FeO, NiO, CoO, MoO_2 and MoO_3 in silicate melts. Chemical Geology 186, 151-181.

O'Neill, H.S.C. and Nell, J. (1997) Gibbs free energies of formation of RuO_2, IrO_2, and OsO_2: A high-temperature electrochemical and calorimetric study.

Geochimica et Cosmochimica Acta 61, 5279-5293.

Paparoni, G., Webster, J.D. and Walker, D. (2010) Experimental techniques for determining tin solubility in silicate melts using silica capsules in 1 atm furnaces and rhenium capsules in the piston cylinder. American Mineralogist 95, 776-783.

Pownceby, M.I. and O'Neill, H.S.C. (1994) Thermodynamic data from redox reactions at high temperatures. IV. Calibration of the Re-ReO_2 oxygen buffer from EMF and NiO+Ni-Pd redox sensor measurements. Contributions to Mineralogy and Petrology 118, 130-137.

Schmidt, C. (2018) Formation of hydrothermal tin deposits: Raman spectroscopic evidence for an important role of aqueous Sn(IV) species. Geochimica et Cosmochimica Acta 220, 499-511.

Schmidt, C., Romer, R.L., Wohlgemuth-Ueberwasser, C.C. and Appelt, O. (2020) Partitioning of Sn and W between granitic melt and aqueous fluid. Ore Geology Reviews 117.

Sidey, V. (2022) On the effective ionic radii for the tin(II) cation. Journal of Physics and Chemistry of Solids 171.

Taylor, R.G., 1979. Geology of Tin Deposits. Elsevier, Amsterdam, p. 543.

Wang, J., Xiong, X., Zhang, L. and Takahashi, E. (2020) Element loss to platinum capsules in high-temperature–pressure experiments. American Mineralogist 105, 1593-1597.

Wang, R.C., Yu, A.P., Chen, J., Xie, L., Lu, J.J. and Zhu, J.C. (2012) Cassiterite exsolution with ilmenite lamellae in magnetite from the Huashan metaluminous tin granite in southern China. Mineralogy and Petrology 105, 71-84.

Wilson, G.A. and Eugster, H.P. (1990) Cassiterite solubility and tin speciation in supercritical chloride solutions. Geochem Soc Special Publ 2:179–195.

Xie, L., Wang, R., Chen, J., Zhu, J., Zhang, W., Wang, D. and Yu, A. (2008) Primary Sn-rich titianite in the Qitianling granite, Hunan Province, southern China: An important type of tin-bearing mineral and its implications for tin exploration. Science Bulletin 54, 798-805.

Xie, L., Wang, R.C., Chen, J. and Zhu, J.C. (2010) Mineralogical evidence for magmatic and hydrothermal processes in the Qitianling oxidized tin-bearing granite (Hunan, South China): EMP and (MC)-LA-ICPMS investigations of three types of titanite. Chemical Geology 276, 53-68.

Xiong, X.L., Adam, J. and Green, T.H. (2005) Rutile stability and rutile/melt HFSE partitioning during partial melting of hydrous basalt: Implications for TTG genesis. Chemical Geology 218, 339-359.

Xu, T., Liu, X.C., Xiong, X.L., Wang, J.T. (2022) Sulfur dissolution capacity of highly hydrated and fluid-saturated dacitic magmas at the lower crust and implications for porphyry deposit formation. Geochimica et Cosmochimica Acta 333, 107–123.

Zajacz, Z., Halter, W.E., Pettke, T. and Guillong, M. (2008) Determination of fluid/melt partition coefficients by LA-ICPMS analysis of co-existing fluid and silicate melt inclusions: Controls on element partitioning. Geochimica et Cosmochimica Acta 72, 2169-2197.

Zajacz, Z., Seo, J.H., Candela, P.A., Piccoli, P.M. and Tossell, J.A. (2011) The solubility of copper in high-temperature magmatic vapors: a quest for the significance of various chloride and sulfide complexes. Geochimica et Cosmochimica Acta 75, 2811–2827.

Zhang, L., Ren, Z.Y., Xia, X.P., Yang, Q., Hong, L.B. and Wu, D. (2019) In situ determination of trace elements in melt inclusions using laser ablation inductively coupled plasma sector field mass spectrometry. Rapid Commun Mass Spectrom 33, 361-370.

Zhao P. L., Zajacz Z., Tsay A. and Yuan S. D. (2022b) Magmatic-hydrothermal tin deposits form in response to efficient tin extraction upon magma degassing. Geochimica et Cosmochimica Acta 316, 331-346.

Zhao, P.L., Chu, X., Williams-Jones, A.E., Mao, J.W. and Yuan, S.D. (2022a) The role of phyllosilicate partial melting in segregating tungsten and tin deposits in W-Sn metallogenic provinces. Geology 50, 121-125.

Figure captions

Fig. 1. Schematic diagrams of the capsule designs for the experiments at different *f*O_2 buffers. **(a)** Single capsule design (design 1) for the Ru–RuO_2 buffered runs, in which the Ru–RuO_2 buffer is directly in contact with the sample. In this design, Pt capsules were used at high temperatures (≥ 1000 °C), and Au capsules at low temperatures (< 1000 °C). This design works very well because Sn does not alloy with the noble metal capsule under this highly oxidizing condition and Ru does not dissolve into the sample. **(b)** Double capsule design (design 2) for the Re–ReO_2 or graphite buffered runs, in which an inner Re capsule was used as the sample container because Sn does not significantly alloy with Re. The Re–ReO_2 or graphite buffers are directly in contact with the sample because they do not react with Sn and show near to no dissolution in the sample. **(c)** Double capsule design (design 3) for the Co–CoO or Fe–FeO buffered runs, in which the sample is loaded into an inner Re capsule and the buffer is loaded between the inner and outer capsules. The Co–CoO or Fe–FeO buffers are added outside of the Re sample capsule because Fe and Co may alloy with Sn and may significantly dissolve into the sample. For design 2 and design 3, sintered ZrO_2 filled the volume between the inner and outer capsules to minimize deformation of the capsules during the experiments.

Fig. 2. Comparison of Sn contents of the quenched glasses measured by EPMA and

LA-ICP-MS, showing consistent results between the two methods. Error bars are displayed only where they are larger than the symbols. Data are provided in Tables 5 and S6.

Fig. 3. Backscatter electron images of representative run products for the capsule designs 1, 2 and 3 as shown in Figure 1. **(a)** Run T5A with design 1 at 900 °C, 0.5 GPa, and Ru–RuO_2 buffered condition, **(b)** Run 21Re with design 2 at 950 °C, 0.5 GPa, and graphite buffered condition, and **(c)** Run 10Re with design 3 at 950 °C, 0.5 GPa, and Co–CoO buffered condition. The results show that (1) euhedral to subhedral titanite (Ttn), ilmenite (Ilm), and scheelite (Sch) coexist with clear quenched glass (Gl), and (2) the fO_2 buffers remain survived after the experiment. The fluid bubbles (Fl) present in the quenched glasses of Run T5A **(a)** and Run 10Re **(c)** indicate melt H_2O saturation.

Fig. 4. Compositions of ilmenite plotted in the FeO–$FeO_{1.5}$–TiO_2 diagram. Dashed lines correspond to the ilmenite–hematite solid solution. Data are from Tables 4 and S3.

Fig. 5. **(a)** D_{Sn} vs. experimental duration (in hours) for time-series experiments at 900 °C, 0.5 GPa, and Ru–RuO_2 buffered conditions. **(b)** Tin content in melt (Sn solubility) vs. temperature for experiments at 0.5-1 GPa and Ru–RuO_2 buffered

condition. Data are from Tables 6 and S8.

Fig. 6. D_{Sn} vs. ΔQFM, temperature and melt NBO/T for titanite **(a, b, c)** and ilmenite **(d, e, f)**, showing that (1) D_{Sn}^{Ttn} and D_{Sn}^{Ilm} decrease with decreasing fO_2 **(a, d)**, and (2) D_{Sn}^{Ttn} and D_{Sn}^{Ilm} decrease with increasing temperature and melt NBO/T in the Ru–RuO_2 buffered runs **(b, c, e, f)**. The dashed red lines in **(a)** and **(d)** were regressed mainly based on 950 °C data following O'Neill and Eggins (2002) $[D_{\Sigma M}^{min/melt} = (D_{M^{n+}}^{min/melt} \cdot K \cdot (fO_2)^{-\frac{1}{2}} + (D_{M^{(n+2)+}}^{min/melt})/(1 + K \cdot (fO_2)^{-\frac{1}{2}})$, where M is a multivalent element, and n is the valence state of the element in reduced form]. The dashed grey lines in **(c)**–**(f)** are regressed based on data from the Ru–RuO_2 or graphite buffered runs. Panel **(d)** shows that $D_{Sn}^{\mathrm{Ilm/melt}}$ from the Fe–FeO buffered run deviates from the D_{Sn}–fO_2 trend, which may have been caused by fO_2 fluctuation during the experiment (see the text for more interpretation).

Fig. 7. D_{Sn} vs. D_{Ti} for titanite **(a)** and ilmenite **(b)**, showing a positive linear relationship for D_{Sn} and D_{Ti} at a given experimental fO_2 (Ru–RuO_2 or graphite buffer), suggesting substitution of Sn^{4+} ↔ Ti^{4+} for both minerals.

Fig. 8. Estimated Sn contents for pre-mineralization Hbl-Bt granitic (in red) and Bt granitic (in blue) magmas using the titanite Sn content and $D_{Sn}^{\mathrm{Ttn/melt}}$ (for details, see the text). The round symbols indicate the Sn contents of melt inclusions from tin-

granites A00 (Audétat et al., 2000), Z08 (Zajacz et al., 2008), and B12 (Borisova et al., 2012). This figure shows that the estimated Sn contents in the Qitianling pre-mineralization magmas (Hbl-Bt and Bt granite) are at the high end of the Sn content in the melt inclusions. The grey dashed line represents the bulk rock Sn content of Qitianling granites that is 25 ppm on average (Xie et al.,2010; Huang et al., 2019).

Tables

Table 1 Compositions of synthetic starting material and Qitianling granite QTL38C.

Starting material (synthetic QTL38C+10%CaTiSiO$_5$+trace elements)						QTL38C	
Major elements (wt%)		Trace elements (ppm)				Major elements (wt%)	
	n=8		n=10		n=10		
SiO_2	63.28(0.19)	Sn	5178(287)	Cs	249(2)	SiO_2	65.72
TiO_2	4.05(0.08)	Nb	279(2)	La	182(1)	TiO_2	1.04
Al_2O_3	12.69(0.08)	Ta	254 (2)	Ce	243(2)	Al_2O_3	13.58
FeO	5.35(0.19)	W	484(6)	Pr	234(2)	FeO	5.74
MnO	0.09(0.04)	Mo	350(13)	Sm	222(2)	MnO	0.10
MgO	1.05(0.02)	Zr	336(5)	Eu	242(2)	MgO	1.37
CaO	4.39(0.08)	Hf	435(3)	Gd	248(2)	CaO	3.27
Na_2O	2.58(0.13)	Li	257(3)	Dy	366(2)	Na_2O	2.95
K_2O	3.65(0.05)	Be	267 (5)	Yb	406(3)	K_2O	3.91
SnO_2	0.66(0.05)	Rb	269(1)				

Major elements and trace elements of the synthetic starting material were analyzed by EPMA and LA-ICP-MS (n = analytical points), respectively. Major elements of Qitianling granite QTL38C are from Huang et al. (2019). Numbers in parentheses are 1 s.d..

Table 2 Experimental conditions and run products.

Run	[I]Capsule design	T (℃)	P (GPa)	[II]H_2O_{in} (wt%)	fO_2 buffer	[III]$fO_{2\ Cal.}$ (ΔQFM)	Duration (hours)	Run product phase proportions (wt.%)	ΣR^2	[IV]Fe loss (%)	[V]Sn loss (%)
1A	a	850	0.5	8	Ru–RuO_2	8.1	312	Gl(86.0)+Ilm(8.1)+Cpx(4.4)+Ttn(1.3)+Cst(0.2)+Fl	0.10	1.37	-
1B	a	850	0.5	5	Ru–RuO_2	8.1	312	Gl(85.8)+Ilm(7.9)+Cpx(4.7)+Ttn(1.4)+Cst(0.2)+Fl	0.08	1.43	-
1C	a	850	0.5	3	Ru–RuO_2	8.1	312	Gl(85.8)+Ilm(7.9)+Cpx(4.6)+Ttn(1.4)+Cst(0.3)+Fl	0.06	1.36	-
T1	a	900	0.5	12	Ru–RuO_2	7.8	24	Gl(91.1)+Ilm(7.6)+Ttn(1.0)+Cst(0.3)+Fl	0.23	1.08	-
T2A	a	900	0.5	12	Ru–RuO_2	7.8	48	Gl(91.1)+Ilm(7.5)+Ttn(1.1)+Cst(0.3)+Fl	0.15	0.00	-
T2B	a	900	0.5	12	Ru–RuO_2	7.8	48	Gl(91.2)+Ilm(7.4)+Ttn(1.1)+Cst(0.3)+Fl	0.04	0.00	-
T3A	a	900	0.5	12	Ru–RuO_2	7.8	72	Gl(91.5)+Ilm(6.8)+Ttn(1.6)+Cst(0.1)+Fl	0.05	0.95	-
T3C	a	900	0.5	12	Ru–RuO_2	7.8	72	Gl(90.8)+Ilm(7.4)+Ttn(1.6)+Cst(0.2)+Fl	0.11	2.21	-
T4A	a	900	0.5	12	Ru–RuO_2	7.8	96	Gl(91.3)+Ilm(7.5)+Ttn(1.0)+Cst(0.3)+Fl	0.11	2.26	-
T5A	a	900	0.5	5	Ru–RuO_2	7.8	120	Gl(91.5)+Ilm(6.8)+Ttn(1.6)+Cst(0.1)+Fl	0.06	1.01	-
T5B	a	900	0.5	10	Ru–RuO_2	7.8	120	Gl(91.6)+Ilm(6.8)+Ttn(1.6)+Cst(<0.1)+Fl	0.04	0.51	-
3A	a	950	0.5	5	Ru–RuO_2	7.5	108	Gl(91.7)+Ilm(7.1)+Ttn(1.0)+Cst(0.2)+Fl	0.10	3.01	-
3B	a	950	0.5	8	Ru–RuO_2	7.5	108	Gl(91.8)+Ilm(7.0)+Ttn(1.1)+Cst(0.2)+Fl	0.06	0.77	-
7M	a	1000	0.5	5	Ru–RuO_2	7.2	96	Gl(94.1)+Ilm(5.7)+Cst(0.2)+Fl	0.10	1.45	-
7D	a	1000	0.5	8	Ru–RuO_2	7.2	96	Gl(93.5)+Ilm(6.3)+Cst(0.2)+Fl	0.06	1.28	-
9A		1000	1.0	10	Ru–RuO_2	7.0	76	Gl(85.3)+Ilm(5.5)+Hem(<0.1) +Ttn(4.3)+Cst(5.0)	0.91	0.00	-
9B		1000	1.0	10	Re–ReO_2	2.1	76	Gl(89.4)+Ilm(1.2)+Rtl(2.7)+Ttn(1.7)+Cst(5.0)	0.28	0.00	-
22Re	b	900	0.5	15	graphite	−1.0	120	Gl(88.1)+Ilm(5.4)+Cpx(5.7)+Rtl(0.3)+Sch(0.5)	0.06	0.21	0.00
21Re	b	950	0.5	15	graphite	−1.1	108	Gl(92.8)+Ilm(4.8)+Cpx(1.8)+Sch(0.7)	0.05	0.00	3.81
28Re	b	1000	0.5	15	graphite	−1.1	96	Gl(98.8)+Ilm(1.2)	0.58	0.00	0.00
10Re	c	950	0.5	12	Co–CoO	−1.1	108	Gl(94.5)+Ilm(4.5)+Ttn(0.5)+Sch(0.5)+Fl	0.55	0.00	46.00
12Re	c	950	0.5	12	*Fe–FeO	> −4.2	108	Gl(94.9)+Ilm(4.2)+Ttn(0.5)+Sch(0.5)+Fl	0.75	0.00	55.70

All the experiments were performed using QT38C + 10%$CaTiSiO_5$ + trace elements as starting materials, except for two runs (9A and 9B with $Au_{99}Sn_1$ capsules as the Sn source), where the starting material was QT38C (dry glass melted from a natural rock powder) + 10% $CaTiSiO_5$ without addition of trace elements. The runs labelled "T" are time-series experiments. Phase abbreviations: Gl: glass; Ttn: titanite; Ilm: ilmenite; Hem: hematite; Cst: cassiterite; Cpx: clinopyroxene; Rtl: rutile; Sch: scheelite; Fl: fluid bubbles. Phase proportions (wt%) were calculated from mass balance. R^2 is the residual of the mass balance calculations.

[I] capsule designs as described in Fig 1a, b, and c (except for runs 9A and 9B, which have the capsule design as in Fig 1a, but $Au_{99}Sn_1$ capsules were used).

[II] initial H_2O content added to the sample capsule.

[III] ΔQFM=logfO_2(experiment) − logfO_2(QFM; Frost, 1991). Buffer materials remained present after the experiments in all but one (run 12Re); fO_2 values were calculated for Ru–RuO_2 (equation of O'Neill and Nell, 1997); Re–ReO_2 (equation of Pownceby and O'Neill, 1994); Co–CoO (equation of Holmes et al., 1986); graphite=CCO (equation of Jakobsson and Oskarsson, 1994); Fe–FeO (equation of Huebner, 1971). Note that Fe in run 12 Re (*Fe–FeO) was consumed after the experiment and the real fO_2 in this run may thus be higher than the Fe-FeO buffer.

[IV] relative Fe loss was calculated by mass balance. Fe loss (%) = (FeO in starting material − FeO calculated in run product)/ FeO in starting material × 100.

[V] relative Sn loss was calculated by mass balance. Sn loss (%) = (SnO_2 in starting material − SnO_2 calculated in run product)/SnO_2 in starting material × 100. Relative Sn loss for the cassiterite saturated runs was not calculated.

Table 3 Rim compositions and Sn contents of titanite analyzed by EPMA (wt%)

Run	SiO_2	TiO_2	Al_2O_3	FeO	CaO	SnO_2	Nb_2O_5	Ta_2O_5	WO_3	ZrO_2	HfO_2	ΣREE	Total	Sn (ppm)
1A	27.05(0.84)	26.96(1.18)	1.19(0.12)	3.37(0.77)	24.13(0.71)	6.46(0.76)	0.53(0.08)	0.42(0.10)	0.74(0.14)	0.43(0.09)	0.70(0.23)	4.99(1.44)	98.38(0.36)	50903(6005)
1B	26.39(0.66)	25.22(1.12)	1.20(0.21)	3.86(0.53)	23.00(0.46)	7.64(0.76)	0.79(0.13)	0.46(0.19)	0.90(0.14)	0.38(0.09)	0.57(0.14)	7.37(1.74)	99.02(0.87)	60191(6017)
1C	26.97(0.68)	26.26(0.89)	1.45(0.18)	3.40(0.51)	22.95(0.57)	6.07(0.86)	0.76(0.06)	0.53(0.13)	0.89(0.13)	0.37(0.12)	0.59(0.21)	7.96(0.86)	99.00(0.21)	47827(6803)
T1	27.39(0.28)	25.41 (0.88)	1.08 (0.08)	3.25 (0.17)	23.22 (0.36)	9.42 (1.33)	0.64(0.1)	0.65(0.18)	bdl	0.29(0.19)	0.39(0.23)	8.09(0.75)	99.29(0.4)	74185 (10509)
T2A	26.10 (0.85)	26.52(0.48)	1.1(0.07)	3.96(1.22)	23.14(0.78)	8.18(0.73)	0.44(0.02)	0.5(0.03)	bdl	0.17(0.03)	0.32(0.02)	9.03(0.48)	99.66(0.3)	64423(5749)
T2B	27.09(0.21)	27.34(0.54)	1.03(0.1)	3.07(0.21)	24.08(0.28)	7.53(0.88)	0.57(0.04)	0.43(0.08)	bdl	0.21(0.06)	0.36(0.09)	7.36(1.02)	99.23(0.72)	59316(6904)
T3A	27.27(0.19)	27.52(0.05)	1.14(0.04)	3.33(0.19)	24.09(0.05)	6.49(0.42)	0.58(0.06)	0.59(0.09)	bdl	0.21(0.03)	0.39(0.04)	6.58(0.69)	98.31(0.11)	51115(3269)
T3C	27.43(0.13)	28.06(0.33)	1.06(0.04)	3.14(0.28)	24.42(0.16)	6.75(0.14)	0.42(0.09)	0.38(0.04)	bdl	0.22(0)	0.43(0.02)	7.62(0.53)	100.05(0.3)	53143(1135)
T4	27.17(0.2)	27.92(0.61)	1.07(0.04)	3.04(0.18)	24.21(0.22)	6.85(0.36)	0.61(0.06)	0.46(0.03)	bdl	0.19(0.03)	0.31(0.05)	7.41(0.74)	99.35(0.44)	53920(2866)
T5A	27.07(0.66)	27.72(0.88)	0.94(0.07)	2.61(0.22)	23.95(0.30)	8.22(0.83)	0.43(0.04)	0.45(0.07)	0.65(0.08)	0.19(0.04)	0.37(0.05)	5.34(0.48)	99.44(0.34)	64724(6542)
T5B	26.56(0.54)	26.25(0.54)	0.87(0.08)	2.62(0.16)	23.49(0.17)	10.28(0.75)	0.38(0.06)	0.52(0.14)	0.68(0.05)	0.18(0.05)	0.39(0.11)	6.06(0.43)	99.54(0.25)	80942(5916)
3A	26.94(0.51)	27.48(0.63)	0.96(0.08)	2.72(0.14)	23.55(0.19)	8.54(0.70)	0.35(0.04)	0.42(0.06)	0.69(0.04)	0.19(0.03)	0.37(0.06)	6.21(0.28)	99.56(0.18)	67301(5485)
3B	27.11(0.73)	27.51(0.66)	0.86(0.09)	2.52(0.23)	23.77(0.10)	9.02(0.78)	0.38(0.06)	0.39(0.08)	0.61(0.04)	0.18(0.03)	0.39(0.05)	5.71(0.12)	99.16(0.23)	71068(6152)
10Re	28.70(0.27)	35.30(0.50)	1.39(0.10)	1.23(0.16)	25.59(0.14)	0.63(0.24)	0.30(0.05)	0.51(0.09)	0.48(0.10)	0.16(0.07)	0.40(0.17)	3.34(0.40)	99.00(0.55)	4964(1875)
12Re	29.57(0.51)	36.13(0.18)	1.54(0.16)	1.20(0.19)	25.51(0.22)	0.14(0.10)	0.34(0.05)	0.47(0.11)	0.62(0.07)	0.15(0.05)	0.33(0.04)	3.32(0.24)	99.92(0.36)	1112(768)
9A	28.02(0.62)	26.43(1.43)	0.65(0.12)	1.74(0.12)	25.35(0.31)	15.14(2.42)	bdl	bdl	bdl	bdl	bdl	bdl	97.64(0.55)	119265(19081)
9B	28.09(0.23)	28.34(0.17)	0.77(0.09)	1.50(0.10)	25.33(0.09)	13.49(0.76)	bdl	bdl	bdl	bdl	bdl	bdl	97.76(0.66)	107330(5720)

The original data are reported in supplementary Table S2. Numbers in parentheses are 1 s.d.. Sn (ppm) in the last column is converted from SnO_2 (wt%) in column 7. bdl means below detection limit (the starting material of runs 9A and 9B was not doped with trace elements).

Table 4 Compositions and Sn contents of ilmenite and rutile analyzed by EPMA (wt%)

Run	Phase	SiO_2	TiO_2	Al_2O_3	FeO	MnO	MgO	CaO	SnO_2	Total	Sn (ppm)
1A	Ilm	0.16(0.09)	39.04(1.33)	1.56(0.26)	46.63(1.28)	0.15(0.02)	3.28(0.28)	0.11(0.07)	2.63(0.51)	93.82(1.28)	20726(3983)
1B	Ilm	0.11(0.02)	40.21(0.77)	1.69(0.12)	46.05(0.66)	0.16(0.02)	3.54(0.19)	0.06(0.01)	2.87(0.26)	94.89(0.73)	22626(2052)
1C	Ilm	0.12(0.02)	39.91(0.90)	1.72(0.07)	46.25(0.57)	0.15(0.02)	3.26(0.20)	0.06(0.02)	2.28(0.34)	93.94(0.56)	17933(2671)
T1	Ilm	0.09(0.03)	39.75(0.39)	1.64(0.15)	45.36(0.61)	0.13(0.04)	3.18(0.19)	0.07(0.04)	2.47(0.13)	92.69(0.46)	19421(1014)
T2A	Ilm	0.13(0.07)	38.59(0.38)	1.67(0.22)	45.80(0.88)	0.11(0.01)	3.11(0.21)	0.10(0.03)	2.30(0.36)	91.83(0.59)	18106(2805)
T2B	Ilm	0.15(0.06)	38.98(1.14)	1.60(0.17)	45.56(1.84)	0.12(0.01)	3.25(0.46)	0.13(0.02)	2.49(0.21)	92.30(0.31)	19634(1641)
T3A	Ilm	0.09(0.01)	40.02(0.68)	1.75(0.05)	44.76(0.47)	0.15(0.01)	3.41(0.23)	0.07(0.02)	2.5(0.15)	92.75(0.62)	19717(1155)
T3C	Ilm	0.15(0.12)	39.57(0.83)	1.62(0.08)	44.58(0.98)	0.14(0.03)	3.46(0.33)	0.11(0.03)	2.52(0.16)	92.19(0.39)	19862(1294)
T4	Ilm	0.14(0.03)	40.85(1.05)	1.68(0.08)	42.9(1.75)	0.14(0.03)	4.05(0.49)	0.11(0.01)	2.43(0.18)	92.30(0.24)	19124(1417)
T5A	Ilm	0.07(0.02)	40.14(0.82)	1.82(0.10)	47.11(0.74)	0.14(0.02)	3.32(0.14)	0.06(0.02)	3.06(0.09)	95.89(1.34)	24072(698)
T5B	Ilm	0.08(0.02)	39.96(0.78)	1.84(0.11)	47.31(0.35)	0.14(0.02)	3.27(0.07)	0.06(0.01)	3.06(0.07)	95.84(1.05)	24072(556)
3A	Ilm	0.11(0.02)	41.83(1.05)	1.90(0.05)	43.90(0.52)	0.16(0.02)	4.08(0.13)	0.08(0.01)	2.43(0.20)	94.70(0.79)	19131(1572)
3B	Ilm	0.12(0.03)	38.03(1.17)	1.73(0.11)	45.27(0.31)	0.14(0.02)	3.77(0.17)	0.07(0.01)	2.58(0.19)	91.95(1.24)	20336(1471)
7M	Ilm	0.08(0.02)	40.46(0.26)	1.70(0.03)	44.05(0.29)	0.12(0.01)	3.47(0.04)	0.12(0.02)	2.49(0.11)	92.86(0.40)	19627(879)
7D	Ilm	0.13(0.02)	39.98(0.36)	1.70(0.04)	43.83(0.24)	0.12(0.01)	3.56(0.08)	0.14(0.02)	2.57(0.15)	92.48(0.20)	20233(1163)
9A	Ilm	0.16(0.04)	33.75(0.41)	1.23(0.03)	48.10(0.66)	0.14(0.01)	1.09(0.04)	0.15(0.02)	5.62(0.08)	89.84(1.06)	44239(618)
9B	Ilm	0.14(0.03)	28.00(0.24)	0.78(0.05)	52.63(0.41)	0.21(0.02)	1.66(0.04)	0.13(0.01)	3.77(0.07)	87.59(0.49)	29678(570)
22Re	Ilm	0.22(0.13)	52.82(0.54)	0.19(0.08)	41.23(2.48)	0.57(0.05)	3.55(0.17)	41.23(2.48)	0.04(0.01)	97.91(2.52)	307(45)
21Re	Ilm	0.15(0.09)	53.12(0.27)	0.14(0.02)	41.66(1.37)	0.55(0.05)	3.51(0.19)	41.66(1.37)	0.03(0.01)	99.87(1.44)	238(86)
28Re	Ilm	0.16(0.1)	53.92(0.37)	0.22(0.03)	39.76(1.22)	0.54(0.05)	4.66(0.08)	39.76(1.22)	0.02(0.01)	100.04(1.49)	163(59)
10Re	Ilm	0.08(0.02)	52.78(0.25)	0.12(0.01)	40.97(1.1)	0.55(0.06)	3.89(0.08)	40.97(1.1)	0.03(0.01)	99.03(0.99)	275(98)
12Re	Ilm	0.1(0.03)	50.12(0.23)	0.17(0.01)	43.04(1.25)	0.52(0.06)	3.77(0.05)	43.04(1.25)	0.11(0.02)	98.39(1.35)	896(169)
9A	Hem	0.19(0.10)	10.34(0.32)	1.32(0.16)	68.65(0.39)	0.32(0.01)	2.24(0.04)	0.23(0.01)	2.18(0.04)	85.44(0.37)	17163(282)
9B	Rtl	0.30(0.09)	68.24(0.68)	0.23(0.05)	2.53(0.06)	0.01(<0.01)	0.04(<0.01)	0.24(0.01)	17.52(0.05)	92.48(1.36)	137982(403)
22Re	Rtl	0.19(0.01)	88.29(1.37)	0.50(0.05)	1.70(0.08)	0.01(0.01)	0.06(0.01)	1.70(0.08)	0.06(0.01)	99.59(1.32)	457(102)

The original data are reported in supplementary Table S3. Numbers in parentheses are 1 s.d.. Sn (ppm) in the last column is converted from SnO_2 (wt%) in column 10.

Table 5 Compositions (wt%) and Sn contents (ppm) of quenched glass analyzed by EPMA and/or LA-ICP-MS

Run	SiO_2	TiO_2	Al_2O_3	FeO	MnO	MgO	CaO	[a]Na_2O	K_2O	SnO_2	Total	[b]H_2O_{melt} (wt%)	[c]Sn (ppm)	[a]Sn (ppm)	[d]NBO/T
1A	64.75(0.58)	0.22(0.02)	13.04(0.15)	0.83(0.10)	0.05(0.03)	0.35(0.03)	3.04(0.14)	2.79(0.01)	3.61(0.10)	0.04(0.01)	89.07 (1.15)	10.93	**323(48)**	**334(7)**	0.035
1B	65.08(0.35)	0.23(0.03)	12.96(0.15)	0.91(0.05)	0.06(0.02)	0.37(0.04)	2.97(0.07)	2.82(0.01)	3.74(0.13)	0.04(<0.01)	89.63 (0.86)	10.37	**299(33)**	**326(14)**	0.037
1C	64.83(0.35)	0.22(0.02)	13.07(0.16)	0.92(0.07)	0.04(0.02)	0.36(0.07)	3.01(0.08)	2.89(0.10)	3.73(0.22)	0.06(0.01)	89.65 (1.11)	10.35	**455(105)**	**466(22)**	0.038
T1	63.31(0.23)	0.52(0.04)	12.84(0.04)	1.49(0.05)	0.06(0.02)	0.83(0.02)	4.12(0.04)	2.56(0.05)	3.21(0.12)	0.1(0.01)	88.31(0.37)	11.69	794(74)	938(45)	0.104
T2A	63.54(0.38)	0.5(0.03)	12.48(0.1)	1.64(0.07)	0.06(0.02)	0.8(0.01)	4.17(0.07)	2.71(0.04)	3.32(0.11)	0.11(0.01)	88.59(0.43)	11.41	872(82)	943(7)	0.118
T2B	63.29(0.43)	0.51(0.04)	12.58(0.1)	1.67(0.09)	0.08(0.02)	0.81(0.02)	4.13(0.09)	2.76(0.04)	3.46(0.13)	0.11(0.02)	88.62(0.47)	11.38	866(143)	919(27)	0.120
T3A	63.05(0.3)	0.49(0.04)	12.56(0.07)	1.68(0.07)	0.08(0.02)	0.78(0.03)	3.97(0.12)	2.7(0.03)	3.45(0.11)	0.12(0.01)	88.01(0.41)	11.99	**927(69)**	**983(17)**	0.111
T3C	63.43(0.15)	0.51(0.04)	12.56(0.17)	1.61(0.09)	0.05(0.03)	0.7(0.01)	3.79(0.12)	2.86(0.04)	3.5(0.09)	0.11(0.01)	88.2(0.4)	11.80	**862(114)**	**869(50)**	0.104
T4A	63.15(0.23)	0.52(0.03)	12.57(0.1)	1.69(0.05)	0.07(0.02)	0.77(0.02)	3.99(0.06)	2.79(0.02)	3.47(0.06)	0.11(0.02)	88.38(0.4)	11.62	**827(164)**	**902(96)**	0.117
T5A	62.51(0.33)	0.68(0.05)	12.31(0.20)	1.74(0.09)	0.06(0.02)	0.78(0.04)	3.83(0.07)	2.74(0.04)	3.50(0.10)	0.14(0.01)	89.98 (0.96)	11.02	**1128(57)**	**1113(11)**	0.099
T5B	62.41(0.56)	0.68(0.05)	12.51(0.32)	1.73(0.14)	0.07(0.02)	0.80(0.05)	3.93(0.16)	2.64(0.03)	3.43(0.11)	0.16(0.01)	89.89 (1.45)	11.11	**1221(41)**	**1220(52)**	0.096
3A	62.40(0.32)	1.00(0.05)	12.33(0.15)	1.89(0.12)	0.06(0.04)	0.77(0.05)	3.97(0.08)	2.69(0.03)	3.38(0.15)	0.19(0.01)	89.29 (1.00)	10.71	**1471(79)**	**1472(28)**	0.110
3B	62.52(0.24)	0.88(0.07)	12.35(0.13)	1.81(0.09)	0.07(0.03)	0.80(0.05)	3.98(0.07)	2.67(0.04)	3.41(0.10)	0.17(0.01)	89.17 (0.83)	10.83	**1359(42)**	**1293(20)**	0.107
7M	60.96(0.50)	1.53(0.15)	11.89(0.17)	2.40(0.18)	0.05(0.03)	0.80(0.03)	4.13(0.12)	2.64(0.04)	3.31(0.08)	0.31(0.01)	88.87 (1.33)	11.13	**2418(74)**	**2111(40)**	0.134
7D	61.66(0.61)	1.33(0.08)	12.27(0.19)	2.19(0.17)	0.07(0.02)	0.78(0.03)	4.12(0.08)	2.72(0.03)	3.38(0.10)	0.25(0.02)	89.70 (1.31)	10.30	**1963(127)**	**1774(20)**	0.121
9A	64.00(0.75)	0.82(0.03)	12.97(0.18)	2.31(0.09)	0.13(0.02)	0.89(0.05)	4.15(0.28)	2.81(0.08)	4.02(0.10)	0.31(0.02)	92.70 (1.62)	7.30	**2454(134)**	**2356(62)**	0.118
9B	62.98(0.80)	1.21(0.04)	12.20(0.11)	4.05(0.34)	0.12(0.02)	0.92(0.07)	3.93(0.24)	2.36(0.03)	3.52(0.11)	0.92(0.02)	92.21 (1.78)	7.79	**7256(147)**	**6716(114)**	0.200
22Re	67.91(0.65)	0.92(0.14)	13.93(0.25)	2.68(0.29)	0.06(0.02)	0.47(0.07)	3.32(0.24)	2.91(0.06)	3.91(0.19)	0.73(0.04)	96.88 (1.93)	3.12	5723(277)	5296(296)	0.127
21Re	64.59(0.54)	1.28(0.06)	13.17(0.13)	3.45(0.28)	0.05(0.02)	0.63(0.05)	3.98(0.13)	2.81(0.05)	3.78(0.11)	0.66(0.04)	94.49 (1.41)	5.51	5191(327)	4777(197)	0.189
28Re	63.32(0.53)	3.40(0.19)	12.82(0.20)	5.63(0.16)	0.09(0.02)	1.20(0.04)	4.07(0.16)	2.61(0.02)	3.36(0.11)	0.71(0.03)	98.22 (1.46)	1.78	5621(256)	5377(164)	0.364
10Re	62.04(0.29)	1.07(0.05)	12.69(0.13)	3.63(0.14)	0.08(0.03)	0.88(0.03)	3.48(0.12)	2.76(0.05)	3.60(0.12)	0.34(0.03)	90.63 (0.99)	9.37	2712(213)	2882(60)	0.170
12Re	62.09(0.44)	1.19(0.05)	12.66(0.17)	3.94(0.20)	0.07(0.02)	0.92(0.04)	3.63(0.08)	2.61(0.04)	3.52(0.09)	0.28(0.02)	90.93 (1.15)	9.07	2226(133)	2304(93)	0.197

Sn contents indicated in bold represent the tin solubility in the melt which are saturated in cassiterite.

The original data are reported in supplementary Table S6. Numbers in parentheses are 1 s.d..

[a]Na_2O (column 9) and Sn (column 15) determined by LA-ICP-MS;

[b] melt H_2O content (H_2O in quenched glass) calculated by 100 minus the EPMA total (Na_2O is from LA-ICP-MS).

[c] Sn (ppm) in column 14 is converted from SnO_2 (wt%) in column 11.

[d] NBO/T, non-bridging oxygens per tetrahedrally coordinated cation. $NBO/T = (2 \cdot X_O - 4 \cdot X_T)/X_T$, in which X_T and X_O are the atomic proportions of tetrahedrally coordinated cations (Si, Al, Fe^{3+}) and oxygen, respectively.

Table 6 Calculated Sn partition coefficients ($D_{Sn}^{\mathrm{min/melt}}$) between mineral and melt.

Run	T(°C)	P(Gpa)	fO_2 (ΔQFM)	NBO/T	$D_{Sn}^{\mathrm{Ttn/melt}}$	$D_{Sn}^{\mathrm{Ilm/melt}}$	$D_{Sn}^{\mathrm{Hem/melt}}$	$D_{Sn}^{\mathrm{Rtl/melt}}$	$D_{Sn}^{\mathrm{Cpx/melt}}$
1A	850	0.5	8.1	0.035	152.2(18.28)	61.97(11.99)			17.47(3.3)
1B	850	0.5	8.1	0.037	184.75(20.2)	69.45(7.01)			15.21(3.86)
1C	850	0.5	8.1	0.038	102.65(15.39)	38.49(6.01)			17.50(4.84)
T1	900	0.5	7.8	0.104	79.11 (11.83)	20.71(1.47)			
T2A	900	0.5	7.8	0.118	68.34(6.12)	19.21(2.98)			
T2B	900	0.5	7.8	0.120	64.53(7.75)	21.36(1.89)			
T3A	900	0.5	7.8	0.111	52.01(3.45)	20.06(1.23)			
T3C	900	0.5	7.8	0.104	61.18(3.76)	22.87(1.99)			
T4A	900	0.5	7.8	0.117	59.79(7.1)	21.21(2.75)			
T5A	900	0.5	7.8	0.099	58.16(5.9)	21.63(0.66)			
T5B	900	0.5	7.8	0.096	66.34(5.63)	19.73(0.96)			
3A	950	0.5	7.5	0.110	45.73(3.83)	13.00(1.1)			
3B	950	0.5	7.5	0.107	54.95(4.84)	15.72(1.16)			
7M	1000	0.5	7.2	0.134		9.30(0.45)			
7D	1000	0.5	7.2	0.121		11.41(0.67)			
9A	1000	1	7.0	0.118	50.62(8.21)	18.78(0.56)	7.28(0.23)		
9B	1000	1	2.1	0.127	15.98(0.89)	4.42(0.11)		20.55(0.36)	
22Re	900	0.5	−1.0	0.189		0.06(0.01)		0.09(0.02)	0.02(0.02)
21Re	950	0.5	−1.1	0.364		0.05(0.02)			0.01(0.02)
28Re	1000	0.5	−1.1	0.170		0.03(0.01)			
10Re	950	0.5	−1.1	0.197	1.72(0.65)	0.10(0.04)			
12Re	950	0.5	> −4.2	0.035	0.48(0.33)	0.39(0.06)			

Numbers in parentheses are the propagated uncertainties(σ) of Sn partition coefficients ($D_{Sn}^{\mathrm{min/melt}} = C_{Sn}^{\mathrm{min}}/C_{Sn}^{\mathrm{melt}}$) calculated as:

$\sigma D_{Sn}^{\mathrm{min/melt}} = [(\sigma C_{Sn}^{\mathrm{min}})^2 / (C_{Sn}^{\mathrm{melt}})^2 + (C_{Sn}^{\mathrm{min}})^2 / (C_{Sn}^{\mathrm{melt}})^4 \times (\sigma C_{Sn}^{\mathrm{melt}})^2]^{0.5}$, where $\sigma C_{Sn}^{\mathrm{min}}$, $\sigma C_{Sn}^{\mathrm{melt}}$ are the uncertainties of C_{Sn}^{min} and C_{Sn}^{melt}, respectively.

Figures

Fig. 1

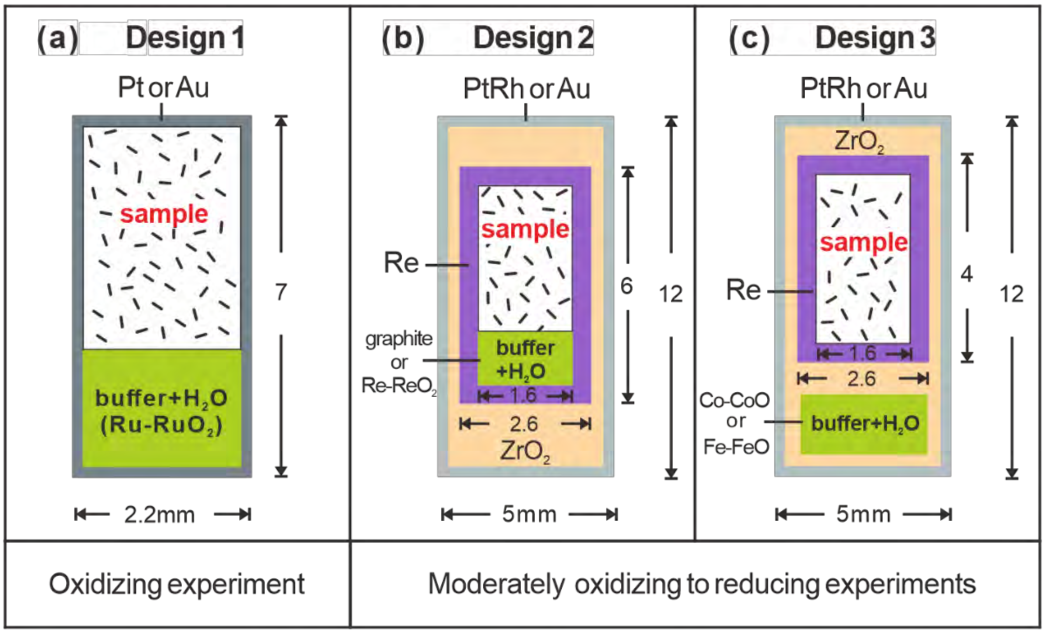

Fig. 2

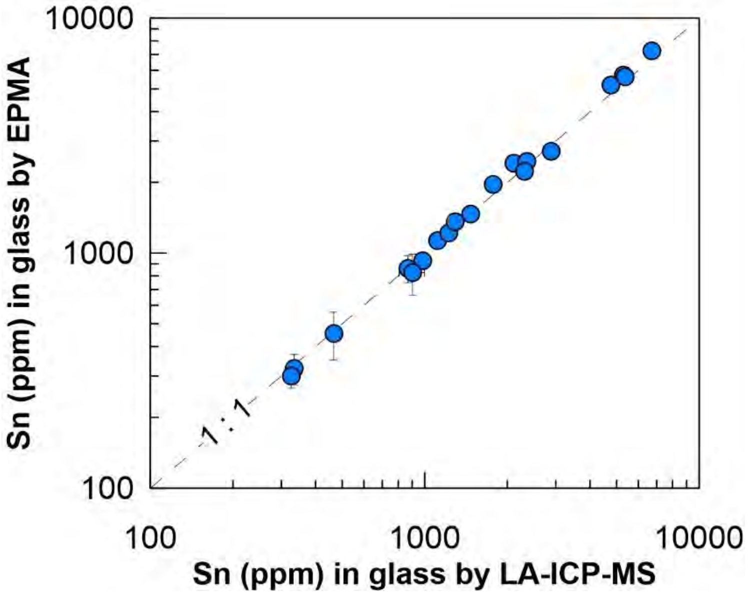
10000
1000
100
Sn (ppm) in glass by EPMA
1 : 1
100
1000
10000
Sn (ppm) in glass by LA-ICP-MS

Fig. 3

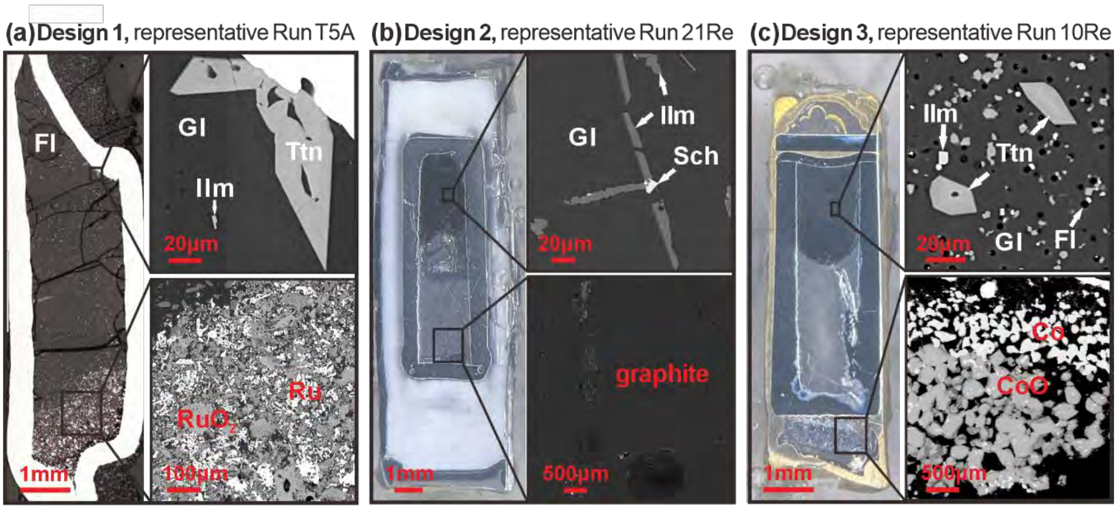
(a) Design 1, representative Run T5A
(b) Design 2, representative Run 21Re
(c) Design 3, representative Run 10Re
Fl
Gl
Ttn
Ilm
20μm
RuO_2
Ru
1mm
100μm
Gl
Ilm
Sch
20μm
graphite
1mm
500μm
Ilm
Ttn
20μm
Gl
Fl
Co
CoO
1mm
500μm

834 **Fig. 4**

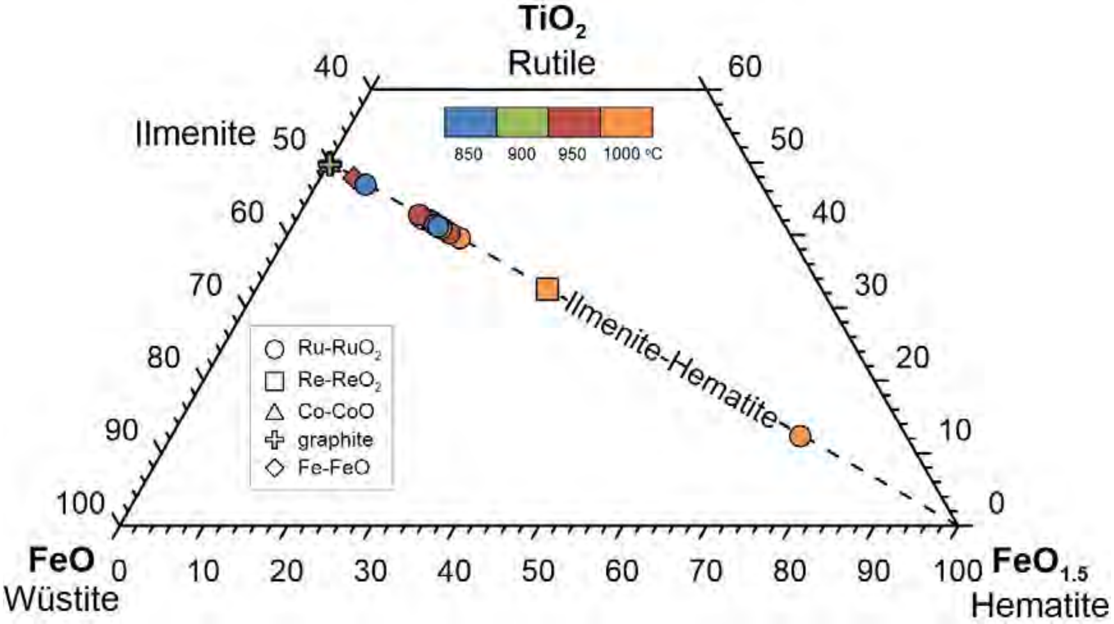

835

836

Fig. 5

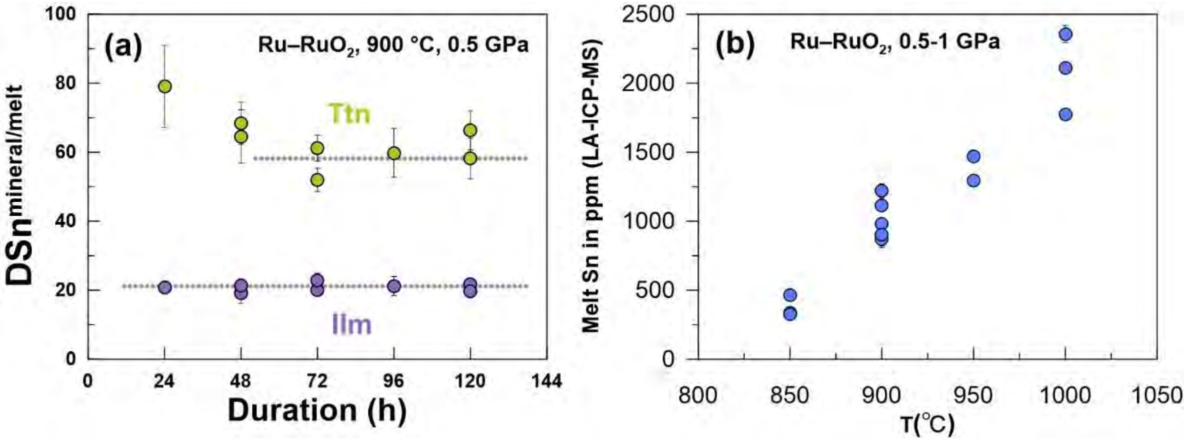
(a)
Ru–RuO$_2$, 900 °C, 0.5 GPa
Ttn
Ilm
DSn$^{mineral/melt}$
0
20
40
60
80
100
0
24
48
72
96
120
144
Duration (h)
(b)
Ru–RuO$_2$, 0.5-1 GPa
Melt Sn in ppm (LA-ICP-MS)
0
500
1000
1500
2000
2500
800
850
900
950
1000
1050
T(°C)

Fig. 6

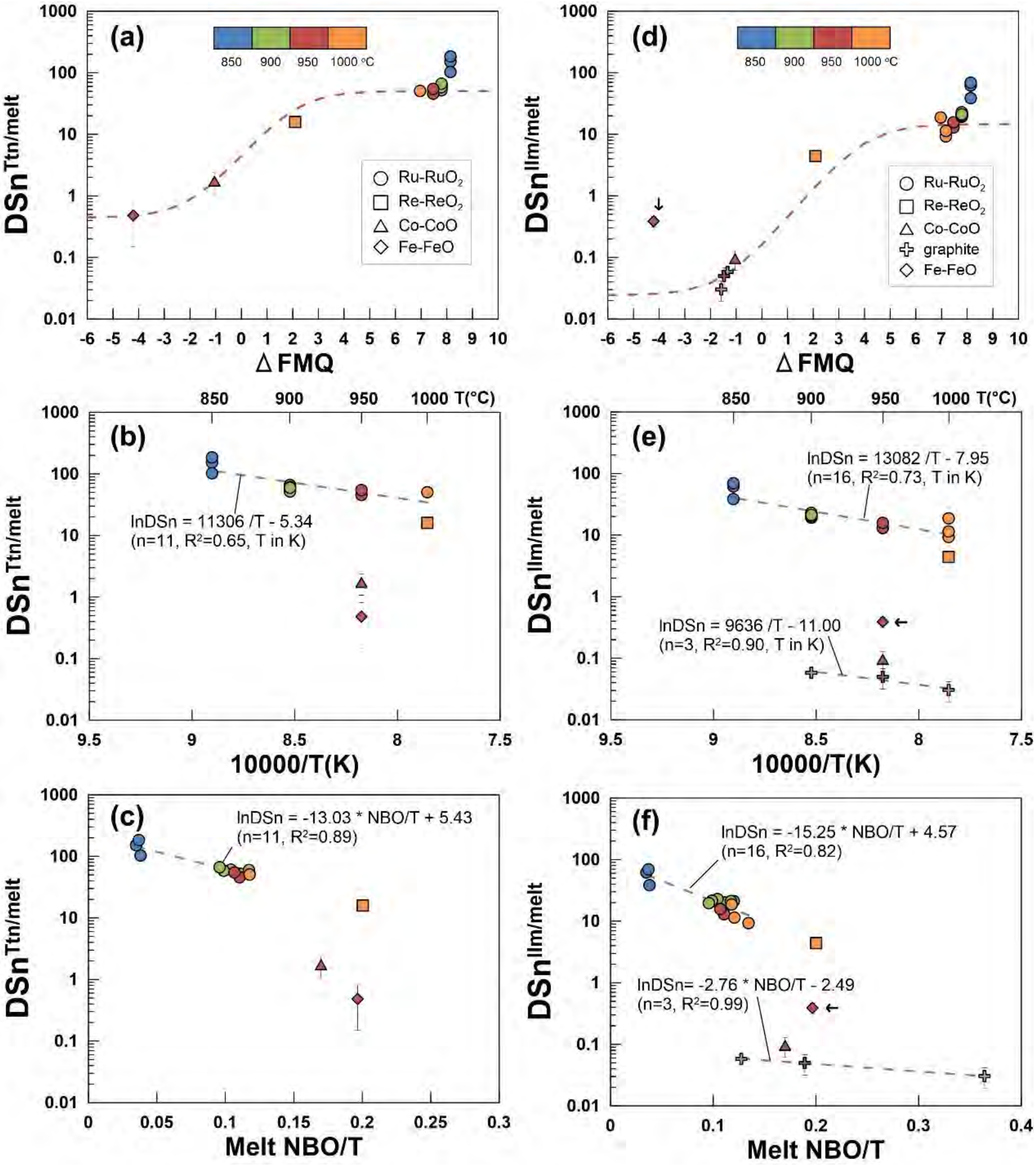
(a)
850
900
950
1000 °C
Ru-RuO2
Re-ReO2
Co-CoO
Fe-FeO
DSn Ttn/melt
ΔFMQ
(d)
graphite
DSn Ilm/melt
(b)
850
900
950
1000 T(°C)
lnDSn = 11306 /T - 5.34
(n=11, R²=0.65, T in K)
10000/T(K)
(e)
lnDSn = 13082 /T - 7.95
(n=16, R²=0.73, T in K)
lnDSn = 9636 /T - 11.00
(n=3, R²=0.90, T in K)
(c)
lnDSn = -13.03 * NBO/T + 5.43
(n=11, R²=0.89)
Melt NBO/T
(f)
lnDSn = -15.25 * NBO/T + 4.57
(n=16, R²=0.82)
lnDSn= -2.76 * NBO/T - 2.49
(n=3, R²=0.99)
0.01
0.1
1
10
100
1000
-6 -5 -4 -3 -2 -1 0 1 2 3 4 5 6 7 8 9 10
9.5 9 8.5 8 7.5
0 0.05 0.1 0.15 0.2 0.25 0.3
0 0.1 0.2 0.3 0.4

Fig. 7

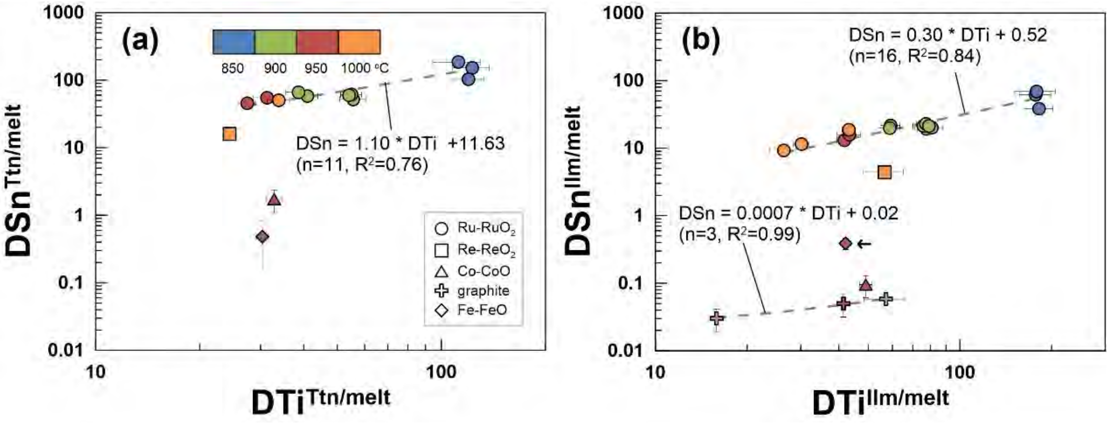
(a)
850
900
950
1000 °C
DSn = 1.10 * DTi +11.63
(n=11, R^2=0.76)
Ru-RuO_2
Re-ReO_2
Co-CoO
graphite
Fe-FeO
1000
100
10
1
0.1
0.01
10
100
$DSn^{Ttn/melt}$
$DTi^{Ttn/melt}$
(b)
DSn = 0.30 * DTi + 0.52
(n=16, R^2=0.84)
DSn = 0.0007 * DTi + 0.02
(n=3, R^2=0.99)
$DSn^{Ilm/melt}$
$DTi^{Ilm/melt}$

847 **Fig. 8**

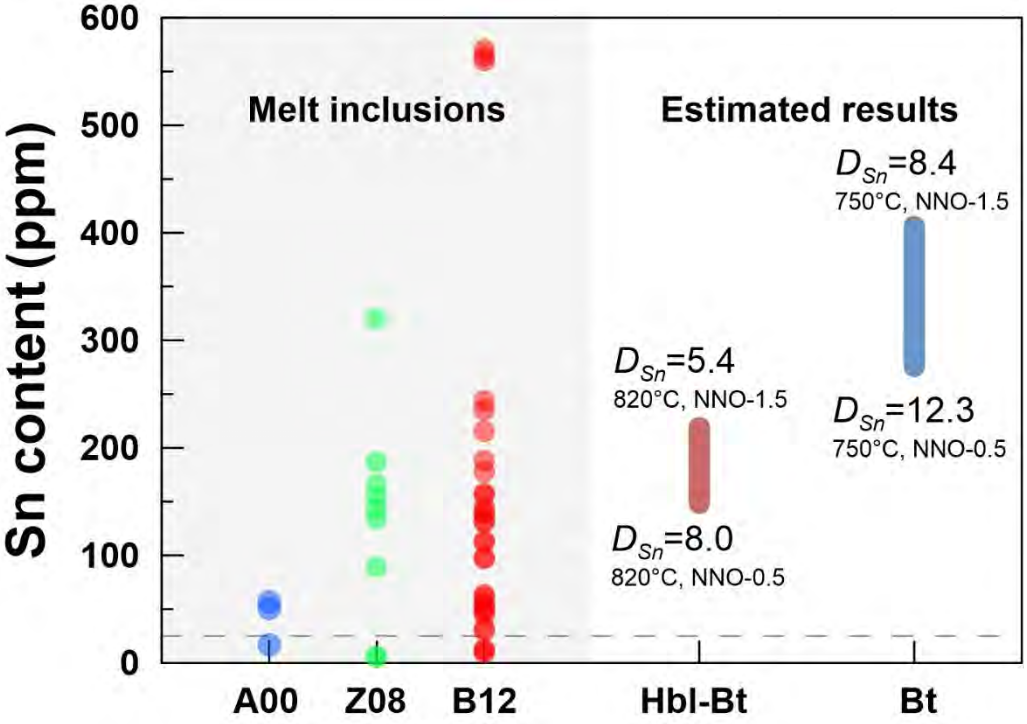
Sn content (ppm)
600
500
400
300
200
100
0
Melt inclusions
Estimated results
D_{Sn}=8.4
750°C, NNO-1.5
D_{Sn}=12.3
750°C, NNO-0.5
D_{Sn}=5.4
820°C, NNO-1.5
D_{Sn}=8.0
820°C, NNO-0.5
A00
Z08
B12
Hbl-Bt
Bt

848